Topological defects in an unconfined nematic fluid induced by single and double spherical colloidal particles

Yiwei Wang and Pingwen Zhang*
LMAM and School of Mathematical Sciences, Peking University, Beijing 100871, People's Republic of China

Jeff Z. Y. Chen†
Department of Physics and Astronomy, University of Waterloo, Ontario N2L 3G1, Canada
(Received 18 April 2017; published 6 October 2017)

We present numerical solutions to the Landau-de Gennes free-energy model under the one-constant approximation for systems of single and double spherical colloidal particles immersed in an otherwise uniformly aligned nematic liquid crystal. A perfect homeotropic surface anchoring of liquid-crystal molecules on the spherical surface is considered. A large parameter space is carefully examined, including those in the free-energy model and those describing the dimer configurations and the background liquid-crystal orientation. The stability of the resulting liquid-crystal defects appearing in the neighborhood of the colloidal dimer pair is analyzed in light of the numerical results for their free energies. A number of scenarios are considered: a free dimer pair in a nematic fluid where the free-energy ground states are described in terms of a phase diagram, and a constrained dimer pair where the interparticle distance and the relative orientation of the distance vector to the nematic director can be manipulated. We pay particular attention to the nonsymmetric solutions, which yield several metastable defect states that can be observed in real systems. The high-precision numerical calculations are based on a spectral method, which is an enabling factor that allows us to compare the subtle difference in the free energies of different defect structures.

DOI: 10.1103/PhysRevE.96.042702

I. INTRODUCTION

Topological defects, which occur in an otherwise homogeneously ordered medium as disruptions of the ordering field, display a wide range of different configurations in the physics of liquid crystals [1–5]. In recent decades, there has been considerable progress in understanding defect structures occurring in a nematic liquid-crystal fluid resulted from the geometric frustrations between a liquid-crystal field and the intrusion colloidal particles. The presence of colloidal particles disrupts the orientational order of liquid crystals locally and leads to the formation of topological defects near the particle's surfaces [6]. The research efforts include direct experimental observations on the defect structures induced by single or multiple particles through suspension of colloidal particles in liquid crystals [7–18], and manipulations of colloidal dimers, which probe the effective interaction energies between the colloidal particles [19–29]. On the theoretical side, models of the free energy of liquid crystals were solved to produce defect structures and energies in various cases [30–55], the induced defects were directly analyzed through the topological arguments [56–58], and at a microscopic level particle-based molecular simulations are also available [40,59–61]. The interdisciplinary topic itself lands on a number of branches in physics, materials science, and mathematics, forming problems of fundamental importance.

The early theoretical studies of this type of system are mostly based on the Oseen-Frank theory [30–38,41], which uses a unit vector field $\mathbf{n}(\mathbf{r})$ to describe the overall orientational properties of the liquid-crystal molecules as a function of the spatial coordinate $\mathbf{r}$. Qualitative features of the defect structures can be established by an examination of the optimal vector field, obtained from minimizing the Oseen-Frank free energy, either numerically [35] or through the trial-function approach [34]. Because of the discrete nature of the magnitude of a unit vector, the theory leads to an abrupt singularity of the vector field at a defect location; the evaluation of the free energy around defects, which requires the spatial derivatives of $\mathbf{n}(\mathbf{r})$, is conceptually difficult and one resorts to, for example, the introduction of a cutoff [43].

The Landau-de Gennes theories describe the liquid crystal's orientational properties by an orientational order-parameter tensor $\mathsf{Q}(\mathbf{r})$, which continuously varies in the vicinity of defect locations and enables the calculation of defect's contribution to the free energy, locally. This is particularly useful, as the short-range field variation is a critical contribution that eventually determines the liquid-crystal mediated interaction in the defect-particle complexes, changing their equilibrium structures. As well, the introduction of such a tensor description overcomes the drawback of the Oseen-Frank description, which specifies directions to a headless vector field. This is a popular approach [39,40,43–55] and is also adopted here. Within the one-constant approximation, the structural properties are dominated by two reduced parameters, a reduced temperaturelike parameter τ and a reduced coherence length ξ_R, which is basically the ratio between the distortion rigidity of the liquid crystal and the particle's radius. Section II is a brief account of the Landau-de Gennes theory used in this work.

It is now widely verified experimentally that when a single spherical particle is immersed in a nematic liquid crystal, two possible defect configurations can occur in the presence of strong homeotropic surface anchoring [7–9,12,19]. This came as a crucial testimony of the success of some of the theoretical

*pzhang@pku.edu.cn
†jeffchen@uwaterloo.ca

tools used in studying these systems [30,33–36,39,41–43]. In both cases, the defects form a circular line, located either outside the equator of the sphere (a Saturn-ring structure) or at the top of the north pole coaxial with the sphere (a dipole structure). The qualitative features of these structures are reasonably well understood presently. In a typical theoretical study, this is based on a solution of the minimization problem in which the Landau-de Gennes free energy is treated as a functional of $\mathsf{Q}(\mathbf{r})$. The radius of the defect ring of the dipole structure, for example, is relatively small in comparison with the spherical radius; a high-precision numerical solution is required to distinguish it from a point defect at the similar location as it was initially proposed for the dipolelike structure [39]. As a prelude to the much more complicated case of two immersed spherical particles (the dimer problem), in Sec. III we present a defect phase diagram in terms of τ and $1/\xi_R$ under the one-distortion-constant assumption.

The major body of this paper provides a systematic theoretical study of all possible liquid-crystal defect structures that can be stabilized in a dimer problem. This is a system that has been widely explored in the literature and multiple configurations have been proposed [7,11,14–17,19,26,40,44–48,50,52,62]. On top of the structures that can be traced back to possible combinations of single-sphere structures, the sphere-to-sphere distance vector in relationship with the far-field nematic director becomes a critical factor that influences the final outcome of the structures [26,44]. Using the Landau-de Gennes theory, we thoroughly search the parameter space including the parameters associated with this vector-director relationship and describe the stability of defect phases and the evolution of the phase transitions between them; these are aspects that have not been adequately addressed in the literature and are important issues in relationship with structures appearing in real three-dimensional systems.

In the current study, we assume that the spherical particles are immersed in a liquid-crystal bath of infinite size. Other factors that could significantly contribute to real systems are not considered here and these could severely affect our comparison with experiments and simulations of nematic colloids. Among these, most experimental observations have been conducted in confined environments, not in a three-dimensional bulk, to enable direct visualization [7,9,11–14,19–22]; the confinement can affect the equilibrium location of defects [37,41], the stability of each configuration [9,12,17,37,41,63], and the fluid-mediated interaction [21,64–66], especially when the thickness of nematic layer is small. It is also believed that the surface anchoring energy can play a crucial role in establishing the structures of defects [35,36,55], their stabilities [8,35,36], and the fluid-mediated interaction [28,50,52]. We start by summarizing our findings in Sec. IV and then dissect each case individually in relationship with previous theoretical and experimental studies in Secs. V–VIII.

Over the wide parameter space, our study is based on a high-precision numerical solution to the minimization problem. From the computational perspective, one of the difficulties in performing numerical study of this type of systems is that the size of the defect core and the size of colloidal particles could be largely different [39,67]. The finite-difference [14,40,48] and finite-element [39,43,50,68] methods were popular choices to divide the considered region of the studied space into a mesh system on which the tensor function $\mathsf{Q}(\mathbf{r})$ can be represented. To capture the detailed defect information, and hence the free energy of the entire system used for determination of the phase diagram, a refined mesh is required; for a nonaxisymmetric system considered here, in three dimensions the computational cost would be high for an accurate free-energy calculation by using these methods. To combat this problem, here we adopt the spectral method [69], by expanding the three-dimensional tensor function $\mathsf{Q}(\mathbf{r})$ in terms of the orthonormal special functions and treating the unknown expansion coefficients as minimization variables. This method can be used to solve the current problem efficiently in high accuracy, including systems where attention needs to be paid to both contrasting large and small length scales. It enables us to investigate the physical problems in more depth with free energies determined for various structures. We note that Armas-Pérez *et al.* have recently explored another numerical idea—the free energy can be minimized through a Monte Carlo procedure, which explores the landscape stochastically and is different from the traditional, deterministic minimization techniques [70].

As with other deterministic approaches, the current numerical algorithm solves the minimization problem by providing a configuration of the $\mathsf{Q}(\mathbf{r})$ field corresponding to a free-energy minimum, when the system parameters such as τ and ξ_{R} are specified. In a complex free-energy landscape, this can be a local or global minimum. For consideration of the so-called phase diagrams in terms of τ and ξ_{R}, stable states with the (presumably) global energy minima are described (see Secs. III and IV). Metastable states, which correspond to local minima in a theoretical model, are still significant here, as a real system can be trapped in such states and become observable experimentally (Sec. IV). The numerical method allows us to set constraints on the system such as the center-to-center distance of the dimer particles and the far field nematic director. With these constraints and a suitable initial guess, we can determine how a trapped local minimum moves as a function of these constraints. This provides a mechanism to study stability of the final states, as well as the kinetic pathways that the system must go through to achieve a final state (with the assumption that the system is trapped at a local minimum at each time frame) (see Sec. V). To find a metastable state, we can prepare the initial guess by a suitable ansatz function or by starting with a random field. The former traps the minimization procedure in a desirable state (see, for example, in Refs. [44,46]) and the latter is numerical quenching from a random state, which could be viewed qualitatively as thermal quenching, although temperature is not directly involved in the numerical procedure (see, for example, in Refs. [14,48,49]).

II. LANDAU-DE GENNES THEORY

Within the Landau-de Gennes theory for liquid crystals, the orientational ordering is described by the traceless Q tensor, which has 3×3 elements. In a nematic fluid typically represented by a liquid made of rodlike molecules (although the theory itself ignores the shape of molecules making up the fluid), the axial direction of a rod, as the measurement of rod orientation, can be stated by a unit vector $\mathbf{u}$. In the vicinity of a spatial point specified by a positional vector $\mathbf{r}$,

the molecular axes point to different directions and can be collectively described by an orientational distribution function. In terms of the vector notation, the Q tensor is defined by

$$\mathsf{Q}(\mathbf{r}) = \left\langle \mathbf{uu} - \tfrac{\mathsf{I}}{3} \right\rangle, \tag{1}$$

where the spatial dependence of Q is maintained after the average $\langle \ldots \rangle$ is taken over the orientational distribution function. In a spatially inhomogeneous system, such a distribution function has an $\mathbf{r}$ dependence, and hence, Q is a function of $\mathbf{r}$. Here, I is a diagonal 3×3 unit tensor and a tensor product is taken between the two unit vectors. An element of this 3×3 symmetric and traceless matrix is denoted below by Q_{ij} where in a typical Cartesian system, $i = x, y, z$ [1].

A. Free energy

Rather than dealing with the complete $\mathbf{r}$ and $\mathbf{u}$ dependencies of a distribution function of molecules, the Landau-de Gennes theory assumes that the structure of a spatially inhomogeneous nematic liquid crystal can be represented by the tensor field $\mathsf{Q}(\mathbf{r})$ where the orientational properties at $\mathbf{r}$ are reflected by the properties of the Q tensor. Phenomenologically, the free energy contains two parts,

$$F[\mathsf{Q}(\mathbf{r})] = \int [f_{\rm b}(\mathsf{Q}) - f_{\rm b,0} + f_{\rm e}(\mathsf{Q}, \nabla \mathsf{Q})] d\mathbf{r}, \tag{2}$$

where the integration is carried over the region filled with the nematic liquid crystal. The free energy is a functional of the function $\mathsf{Q}(\mathbf{r})$, which can be determined after the free energy is minimized with respect to this tensor function, for a specific problem. The $\mathbf{r}$-independent constant $f_{\rm b,0}$ is the free-energy density of the spatially uniform reference state, given in Eq. (14) below.

The bulk free-energy density is written in an expansion of Q after truncation at the fourth order,

$$f_{\rm b}(\mathsf{Q}) = \frac{A}{2}{\rm tr}(\mathsf{Q}^2) - \frac{B}{3}{\rm tr}(\mathsf{Q}^3) + \frac{C}{4}[{\rm tr}(\mathsf{Q}^2)]^2, \tag{3}$$

where trace (tr) is taken on a matrix, and $\mathsf{Q}^2 = \mathsf{Q} \cdot \mathsf{Q}$ as well as $\mathsf{Q}^3 = \mathsf{Q} \cdot \mathsf{Q} \cdot \mathsf{Q}$ are tensor matrix products. The coefficients A, B, and C are material-dependent parameters.

The elastic free-energy density is commonly written as [71],

$$f_{\rm e}(\mathsf{Q}, \nabla \mathsf{Q}) = \frac{L_1}{2} Q_{ij,k} Q_{ij,k} + \frac{L_2}{2} Q_{ij,j} Q_{ik,k} + \frac{L_3}{2} Q_{ik,j} Q_{ij,k} + \frac{L_4}{2} Q_{kl} Q_{ij,k} Q_{ij,l}, \tag{4}$$

in which the notation $Q_{ij,k}$ refers to a spatial derivative of the element $Q_{ij}(\mathbf{r})$ with respect to the kth spatial variable. In principle, to completely analyze the nematic structure, we must consider this expression with the presence of all material-dependent coefficients L_i. In the so-called one-constant approximation, it is customary in the literature to consider the first term only by letting $L_1 = L$ and $L_2 = L_3 = L_4 = 0$, which neglects possible effects of the elastic anisotropy in liquid crystals. We follow this approximation in the current work.

The current work is concerned with the immersion of (hard) spherical particles of radius R in a nematic fluid; the radius can be conveniently used to reduce physical quantities in the system. We use a dimensionless spatial variable

$$\mathbf{r}' \equiv \mathbf{r}/R, \tag{5}$$

dimensionless system parameters

$$\tau = \frac{27AC}{8B^2} \tag{6}$$

and

$$\xi_R^2 = \frac{27CL}{8B^2R^2}, \tag{7}$$

reduced Q tensor

$$\mathsf{Q}' = \sqrt{\frac{27C^2}{8B^2}}\mathsf{Q}, \tag{8}$$

and reduced free energy

$$F' = \frac{27^2C^3}{2^6B^4R^3}F. \tag{9}$$

Dropping all primes on the reduced symbols with the understanding that we have adopted these scalings, we write

$$f_{\rm b}(\mathsf{Q}) = \frac{\tau}{2}{\rm tr}(\mathsf{Q}^2) - \frac{\sqrt{6}}{4}{\rm tr}(\mathsf{Q}^3) + \frac{1}{4}[{\rm tr}(\mathsf{Q}^2)]^2, \tag{10}$$

and

$$f_{\rm e}(\mathsf{Q}, \nabla \mathsf{Q}) = \frac{\xi_R^2}{2} Q_{ij,k} Q_{ij,k}. \tag{11}$$

This free-energy expression, including (2), (10), and (11), is exactly the same as the one used in Refs. [44,46,62,72].

B. Bulk phase

Here we review the main result of the isotropic-nematic transition in a spatially homogeneous system, for which $f_{\rm e} = 0$ and all $\mathbf{r}$ dependence can be dropped in (10). The minimization of the free energy produces a uniaxial solution where a nematic director $\mathbf{n}$ can be defined. In this case the Q tensor can be represented in a simple form, $\mathsf{Q} = \frac{S_0}{2}(3\mathbf{nn} - \mathsf{I})$, where S_0 is an orientational order parameter [6,73,74]. The system has a first-order isotropic-nematic transition at

$$\tau_{\rm in} = 1/8. \tag{12}$$

Above $\tau_{\rm in}$, the isotropic state is stable and we have $S_0 = 0$ and $f_{\rm b,0} = 0$. Below $\tau_{\rm in}$, the nematic state is stable and we have

$$S_0 = \sqrt{\frac{2}{3}}\left(\frac{3 + \sqrt{9 - 64\tau}}{8}\right) \tag{13}$$

and

$$f_{\rm b,0} = \frac{3\tau}{4}S_0^2 - \frac{3\sqrt{6}}{16}S_0^3 + \frac{9}{16}S_0^4. \tag{14}$$

The isotropic-nematic transition is represented in Fig. 1 by the horizontal line at $\tau = 1/8$.

C. Surface anchoring

Our main concern is the insight into the nematic ordering field represented by $\mathsf{Q}(\mathbf{r})$ in the presence of spherical particles. In this paper, we consider the homeotropic alignment of liquid-crystalline molecules only and leave other types of alignment

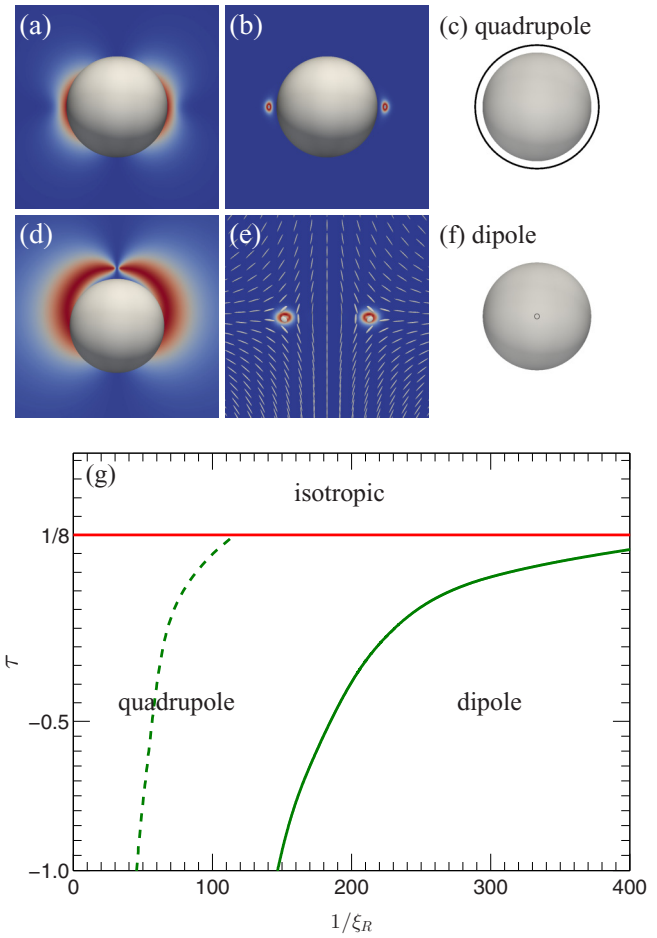

FIG. 1. Defect configurations in a nematic liquid crystal surrounding a spherical particle: (a)–(c) quadrupolar (Saturn-ring) state, (d)–(f) dipolar state, as well as the corresponding regimes in the phase diagram (g) where these states have the lowest free energies. Each state is illustrated by using three views: side views of the $\mathbf{Q}$-tensor element Q_{xx} [in (a) and (d)], the same side views of the biaxiality coefficient β [in (b) and (e)], and top view of the defect location, indicated by the black circles produced from plotting the isosurface of $c_l = 0.1$. (e) is an enlarged version of the defect area on top of the sphere, where the tensor field (white ellipsoids) indicates a $-1/2$ defect line. The reduced parameters used in producing these configurations are: $[\tau,\xi_R] = [-0.2234,0.07209]$ and $[-0.2234,0.007071]$ ($R \approx 0.1\ \mu$m and $R \approx 1\ \mu$m in 5CB) for the quadrupolar and dipolar states, respectively. The dashed line in (g) represents the stability limit of the dipolar state.

for future work. This entails a rodlike molecule prefer to align perpendicularly to the surface of a spherical particle.

More specifically, we consider a Dirichlet boundary condition such that at any given parameter pair τ, ξ_R, the tensor field $\mathbf{Q}(\mathbf{r})$ is required to exactly match a surface field defined by $\mathbf{Q}_s(\mathbf{r}) = \frac{S_0}{2}(3\hat{\mathbf{r}}\hat{\mathbf{r}} - \mathbf{I})$ at the spherical surface, where $\hat{\mathbf{r}}$ is the surface normal direction. Computationally, this is realized by introducing an energy-penalty term (surface energy) when $\mathbf{r}$ is a point on a spherical surface,

$$F_s = \frac{w}{2}\int |\mathbf{Q}(\mathbf{r}) - \mathbf{Q}_s(\mathbf{r})|^2 dA, \tag{15}$$

where the integration is carried over the spherical surfaces containing the surface element dA. This penalty term is considered together with F as we minimize the combination $F + F_s$ with respect to $\mathbf{Q}(\mathbf{r})$. All the results presented below are obtained by letting $w \gg 1$ so that the Dirichlet condition is numerically satisfied in high precision. The exact choice of w, as long as it is large, has a negligible effect on the free-energy data presented in this work. Our computational approach here is the same as or similar to previous treatments of liquid-crystal surface anchoring [39,40,43–46,62,72].

Although our focus is the Dirichlet boundary condition, our numerical method could be used to study the effects of a finite w as an additional system parameter. Indeed, in real systems, it has been argued that the anchoring strength influences the defect properties, such as the equilibrium locations of defects [35,36,55], the stability of the defect structures [8,35,36], and the fluid-mediated interaction between the instructing particles [28,50,52]. There is an expectation that these effects are more profound in systems with nanoscale particles [27,28,52,75]. For example, the theoretical studies by Stark indicate that the quadrupole structure is more stable and the Saturn ring moves closer to the particle surface, at a weaker surface anchoring [35,36]. These theoretical results are in agreement with the experimental observation conducted by Mondain-Monval *et al.*, who observed a transition from the dipole to quadrupole structures for a particle with radius $R = 50$ nm, after decreasing the anchoring strength [8]. The numerical study of Tomar *et al.* based on the Landau-de Gennes theory demonstrated that the magnitudes of interactions between nanoparticles in a nematic liquid crystal are sensitive to the anchoring energy.

Adding w as another parameter dimension is a natural extension of the current work; here we focus on the idealized case of a Dirichlet boundary condition. The comparison between our numerical results and real systems where the boundary condition is not ideal, can be only qualitative.

D. Numerical method

The details of the numerical method can be found in the Appendix and are summarized here. We use the spectral method to minimize the free energy, which is a functional of the tensor function $\mathbf{Q}(\mathbf{r})$. The target function $\mathbf{Q}(\mathbf{r})$ is expanded in terms of proper basis functions after the appropriate identification of a coordinate system. Neglecting the high-order terms in a truncated series, we express the free energy in terms of undetermined coefficients.

A multivariable minimization scheme is then used to minimize the free energy with respect to these coefficients, now as variables. A deterministic procedure such as the limited-memory Broyden–Fletcher–Goldfarb–Shanno algorithm (L-BFGS) [76] is handy to achieve this goal. Standard computational packages are available for this purpose.

After specifying all system parameters such as τ and ξ_R, we are required to find the free-energy minimum. Depending on the initial guess for $\mathbf{Q}(\mathbf{r})$, the numerical system can converge to a local or global minimum, giving rise to a defect structure. To analyze the stability of a particular defect state, sometimes

we take an existing solution as an initial guess for a different region of the parameter space.

E. Selection of parameters

There are two basic parameters in the current model. The reduced free energy only contains reduced parameters τ and ξ_R. While we examine a large range of these parameters generally in this paper, here we specifically take 5CB liquid crystal as an example to make sense of the range in real units.

At the room temperature, it is customary to adopt the parameters $A = -0.172 \times 10^6$ Jm^{-3}, $B = -2.12 \times 10^6$ Jm^{-3}, $C = 1.73 \times 10^6$ Jm^{-3}, and $L = 4 \times 10^{-11}$ Jm^{-1} [6,12,14–17,48,50]. This prompts us to conduct most calculations by setting

$$\tau = -0.2234 \quad \text{(room temperature for 5CB)}. \tag{16}$$

It is generally assumed that $A = a(T - T^*_{NI})$, where T^*_{NI} is the surpercooling temperature [6], hence $\tau = \tilde{a}(T - T^*_{NI})$ from (6). For 5CB, assuming that $\tau = -0.2234$ corresponds to $T_{\text{room}} = 25\,^\circ$C and that $\tau = \frac{1}{8}$ corresponds to $T^* = 35\,^\circ$C [77], we have

$$\begin{aligned} T &= T^* - \frac{T_{\text{room}} - T^*}{0.3484}(\tau - 0.125) \\ &\approx (31.38 + 28.99\tau)\,(^\circ\text{C}) \quad \text{(for 5CB)}. \end{aligned} \tag{17}$$

The pure 5CB undergoes a phase transition from a nematic phase to a crystalline at about $T = 22.5\,^\circ$C [77]; so strictly speaking, for 5CB the lower bound of τ is -0.3063. While in most cases, we stay with $\tau = -0.2234$ in (16), we also extend our study to the range $[-1, 1/8]$, in Secs. III and VI, to illustrate the general trend and to accommodate possible τ range in other materials.

Another important parameter is the coherence length ξ_R in (7). For a given material where B, C, and L are fixed, it can be viewed as the inverse radius of the intruding particle in reduced units. Hence, below we also refer to $1/\xi_R$ as the reduced radius directly. For 5CB, this implies that $\xi_R = 0.07209$ for a particle of radius $R = 0.1\ \mu$m, or the relationship

$$R = 0.007209\xi_R^{-1}\ (\mu\text{m}) \quad \text{(in 5CB)}. \tag{18}$$

The range we considered $[0,400]$ for $1/\xi_R$ is approximately the range $[0,3]$ (μm) for a spherical particle in 5CB.

The mappings in (16)–(18), of course, are material-dependent. Some of physics described below could be observed at different length scales and temperatures when other liquid-crystal materials are used.

F. Visualization of defect structures

The solution to the Landau-de Gennes theory yields an optimal tensor field $\mathbf{Q}(\mathbf{r})$, which is reasonably smooth over the entire space outside the spherical particles. The location of nematic defects in this region, if any, can be detected by the singularities of the eigenvector corresponding to the largest eigenvalue, S, of this 3×3 tensor [78]. The following physical quantities are considered in visualization.

The first is an element of the tensor $\mathbf{Q}(\mathbf{r})$, such as $Q_{xx}(\mathbf{r})$, the values of which are nearly constant in the far field but change significantly near a particle. The colors in all displays are arranged such that the high to low values correspond to variations from red to blue.

A biaxial distribution of the molecular orientations can also be used to detect the existence of the topological defect in this problem. An effective way to measure the biaxial effects is to introduce a biaxial coefficient, our second physical quantity, which is defined by [79]

$$\beta(\mathbf{r}) = 1 - 6\frac{[\text{tr}\mathbf{Q}^3(\mathbf{r})]^2}{[\text{tr}\mathbf{Q}^2(\mathbf{r})]^3}. \tag{19}$$

One can show that $0 < \beta \leqslant 1$ in the biaxial regions and $\beta = 0$ in the uniaxial region. Again, all color displays are arranged such that the high to low values correspond to variations from red to blue.

At a given point represented by $\mathbf{r}$, the tensor field $\mathbf{Q}(\mathbf{r})$ can be diagonalized to form three principal directions. In some illustrations, white ellipsoids with axes along the three principal directors are plotted in selected locations. The most obvious feature of such a plot is the long axes that indicate local nematic directors.

The largest eigenvalue (in magnitude) of the tensor $\mathbf{Q}(\mathbf{r})$ defines the orientational order parameter $S(\mathbf{r})$. The defect line can be visualized by the isosurface of the orientational order parameter $S(\mathbf{r})$ [6] or the isosurface of the Westin metric c_l, which is the difference between the two largest eigenvalues [80]. The resulting effect is a thick, connected curve.

III. SINGLE SPHERICAL PARTICLE IN A NEMATIC FLUID

We first present the phase diagram for the relatively simple single-particle problem, which provides a basis for the analysis of the two-particle problem. With strong homeotropic anchoring, two types of defect configurations arise, containing defect structures of quadrupolar (the so-called Saturn-ring structure) and dipolar states, both being illustrated in Fig. 1. With the bulk nematic director pointing in the vertical direction, the defect ring is located near the spherical equator in the first case, and near the spherical top in the second case.

The Saturn-ring defect structure was predicted by Terentjev theoretically for the current problem [30]. It contains a defect ring curve encircling the axis of the spherical particle. The entire $\mathbf{Q}(\mathbf{r})$ tensor has an axisymmetry about the z axis and reflection symmetry with respect to the x-y plane through the spherical center [see Fig. 2(a)]. The functions used in plotting the illustration, Q_{xx} and β, were produced from the numerical minimization of the Landau-de Gennes model. The location of the Saturn ring is a line defect, around which the nematic director field forms a $-1/2$ topological disclination [see Figs. 1(b) and 1(c)].

The dipolar solution has been known to exist in this system for a long time, with an axisymmetric configuration of $\mathbf{Q}(\mathbf{r})$ that contains no reflection symmetry with respect to the x-y plane [7,34,39]. Previous studies based on the Oseen-Frank theory suggested that the nematic directors form a typical hyperbolic hedgehog pattern about a single point defect, with a winding number -1 in a cross section [34]. This configuration can be obtained from the free-energy minimization of the Landau-de Gennes model, by mathematically enforcing $\mathbf{Q}(\mathbf{r})$ to be uniaxial in the entire space.

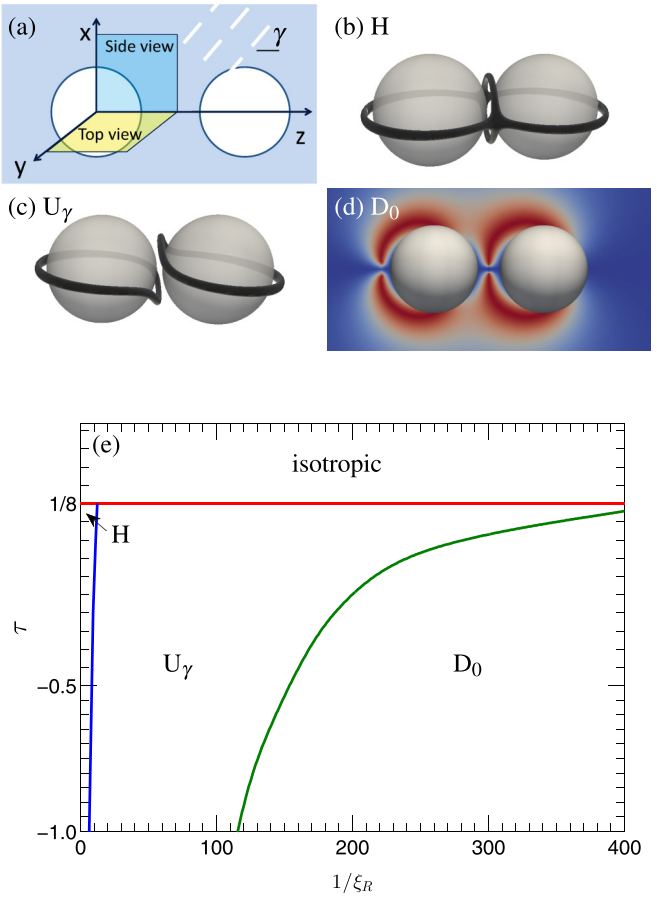

FIG. 2. (a) Sketch of the coordinate system for a dimer problem; (b) entangled hyperbolic defect (H) state where $\gamma = \pi/2$; (c) unentangled defect rings (U_γ) where $\gamma \neq \pi/2$; (d) parallel dipole-dipole state (D_0) where $\gamma = 0$; and (e) the phase diagram that describes the regimes where these defect states have free-energy minima in terms of a reduced temperature τ and reduced spherical radius $1/\xi_R$. The phase diagram was determined based on the ground-state calculation, after consideration of all other possibilities including minimization with respect to the particle distance D and tilt angle γ. (b) and (c) are illustrations of the defect lines determined from isosurface $S = 0.25$. (d) is the cross-section view of Q_{xx}. (b) and (c) are produced from numerical solutions at $[\tau,\xi_R] = [-0.2234,0.07209]$ ($R \approx 0.1$ μm in 5CB). (d) is produced from numerical solutions at $[\tau,\xi_R] = [-0.2234,0.007071]$ ($R \approx 1$ μm in 5CB).

The uniaxial solution, however, is biaxially unstable in the Landau-de Gennes theory as has been pointed out in a number of theoretical studies [81,82]. Using the adaptive finite element method, Fukuda *et al.* showed that the defect region displays a defect ring, co-centered about the z axis [39]. Our current calculation also verifies the ring structure, which can be seen from the illustrations in Fig. 1(d) where the side view Q_{xx} displays a blue gap in the defect region, and the detailed side view of the tensor field clearly indicates a $-1/2$ defect line on spherical top. Once the uniaxial constraint is removed from the minimization procedure, the uniaxial solution gradually evolves to the final biaxial result. The uniaxial solution itself is not a metastable state.

From a comparison of the free energies, the stable state corresponding to the free-energy global minimum can be determined. Shown in Fig. 1(g), a first-order isotropic-nematic phase transition occurs at $\tau_{\text{in}} = \frac{1}{8}$, determined by the bulk free energy. Once the intruding hard particle is introduced, the defect patterns form. The dipolar state is stable in large $1/\xi_R$ systems. Over the region considered in the phase diagram, the quadrupolar pattern can be found, as the stable or metastable state, over the entire parameter space below τ_{in}; the dipolar state can only be found to the right of the dashed curve, which represents the stability limit of this phase. The dipole-quadrupole transition was experimentally produced in 5CB by using a μm-sized gas bubble as a colloid particle with varying radius [13]. Our results suggest that the dipole-quadrupole transition can be induced by a variation of temperature through τ. For fixed $1/\xi_R$, the location of the transition temperature in terms of T for 5CB, can be referred to from the figure and the conversion in (17).

Overall, the phase diagram follows the general principles in phase transitions regarding symmetry breaking. For a fixed ξ_R, as the temperature τ is lowered, the system undergoes phase transitions from a high-symmetry phase (isotropic) to a low-symmetry phase (quadrupolar with axisymmetry and mirror symmetry), and then, to an even-lower-symmetry phase (dipolar with axisymmetry only). Although it has been known for a long time that dipolar solution is energetically preferred for larger particles [36,43], here we present a quantitative phase diagram for ξ_R and τ, which covers a large radius range.

IV. TWO SPHERICAL PARTICLES IN A NEMATIC FLUID: GROUND AND METASTABLE STATES

The emergent nematic defect structures when two spherical particles of equal radii R are placed in a background nematic fluid are rather complicated. In addition to the two parameters τ and ξ_R in the current Landau-de Gennes model, two other parameters are expected to enter the theory: the reduced distance between the centers of the two spherical particles, D/R, and the tilt angle between the center-to-center vector and the far-field nematic director, γ [Fig. 2(a)]. Because of the variety of structures in the single-particle system, a series of recent works suggested that the dimer complex can be composed of dipole-dipole pair [11,15,19,44], quadrupole-quadrupole pair [14,17,40,47,48,50,61], dipole-quadrupole pair [16,62], or even a new bubble-gum structure, which is unique for the dimer case [19,46].

The parameter ξ_R is material related and as such it is fixed when the particle size and liquid-crystal material are selected in an experimental system. The temperaturelike parameter τ depends on the experimental environment and is usually adjusted through temperature and sometimes through density (at least theoretically). Both γ and D/R are configurational parameters, which, in a free system without any constraint, are self-adjusted to yield a free-energy minimum. There are, however, a number of experimental techniques that can be used to fix one or both of these parameters [14,22,26].

Here we describe the ground-state topological defects in the dimer system, after the free energy is minimized with respect to both γ and D/R. Three states, entangled hyperbolic defect (H), unentangled defect rings (U_γ), and parallel dipoles

(D_0), displayed in Figs. 2(b)–2(d), have the lowest free energy in the corresponding regimes of the phase diagram shown in Fig. 2(e). The phase diagram can be compared with the single-particle phase diagram presented in Fig. 1(g).

The stability region of the dipole-dipole pair is very similar in size with that of the single-particle problem. We show in later sections that out of all dipole-dipole configurations, the parallel arrangement with $\gamma = 0$ has the lowest free energy, consistent with the observation made by Poulin *et al.* for μm-sized particles ($R = 1.6 \sim 5\ \mu$m) [19]. Both H and U_γ states are variations of the original, quadrupolar Saturn-ring structure in Fig. 1(a). The size and location of the combined H and U_γ regions in Fig. 2(e) are similar to the phase region where the quadrupolar structure is stable in Fig. 1(g).

Notice that the ground U_γ state determined here has a nontrivial tilt angle γ, which was suggested by several previous studies for μm-sized particles [14,17,48,54]. Qualitatively, due to the fact that the two defect Saturn rings both have the same winding number $-1/2$, the portions of the defect Saturn rings near the sphere-sphere center locally repel each other, following the general principle of defect-defect interactions [1]. As these portions are twisted upwards and downwards, the original spherical axes tilt in order to accommodate a larger distance between these two repelling portions. The value of the optimal γ deviates from $\gamma = \pi/2$ starting from the isotropic-nematic transition line, and increases as the system moves to a low-$1/\xi_R$ state. The exact value of γ that minimizes the free energy depends on the location $[\tau,\xi_R]$ as will be more quantitatively described in Sec. V.

The H state (adapted from "entangled hyperbolic defect" [14,48], also known as "figure of theta" in the literature [56,61,83]) was reported by Guzmán *et al.* based on the Monte Carlo simulations of soft Gay-Berne molecules and a numerical solution to the Landau-de Gennes theory for nanoscale particles [40]. We demonstrate here that it is the only stable configuration in the systems with extremely small $1/\xi_R$ ($R < 68$ nm in 5CB at room temperature). This result is consistent with the numerical study of Hung on the basis of the Landau-de Gennes theory [50], in which no other entangled or unentangled defect structures were found, for nanoparticles with $R = 50$ nm. For a μm-sized particle, the H state was reported by Ravnik *et al.* for $R = 0.5\ \mu$m using the Landau-de Gennes approach in Ref. [14]. By using glass microspheres with radius ranging from $R = 2.35{-}9.5\ \mu$m in 5CB liquid crystal cells with thickness from $5{-}22\ \mu$m, they also successfully observed the H state experimentally [14]. It is possible that H in the above experiment with a rather large R was further stabilized by the finite cell thickness, or it remained intact in a metastable region. Due to the structural symmetry, in particular the mirror symmetry about the x-y plane, the H state is very stable against any perturbations from $\gamma = \pi/2$, as tested by our numerical experiments. The relationship between H and other related $\gamma = \pi/2$ states is addressed in Sec. VII.

Beyond the three free-energy ground states discussed here, out of quite a number of configurations discussed below, six configurations are found metastable, after the free energy is minimized with respect to the liquid-crystal order parameter $\mathbf{Q}(\mathbf{r})$ and dimer configuration-parameters D/R and γ, as illustrated in Fig. 3. The first two were nicknamed "figure of eight" (E) and "figure of omega" (O) previously by

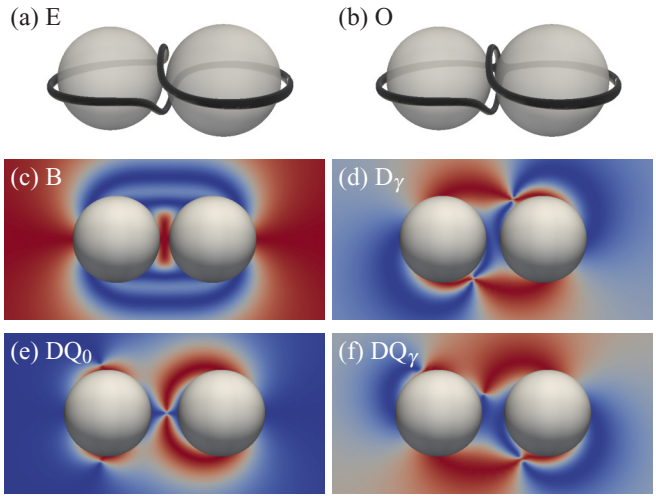

FIG. 3. Metastable colloidal dimer configurations in a nematic fluid determined from the Landau-de Gennes free energy in the current work: (a) figure-of-eight (E), (b) figure-of-omega (O), (c) bubble-gum (B), (d) tilted antiparallel dipoles (D_γ), (e) axisymmetric dipole-quadrupole (DQ_0), and (f) asymmetric dipole-quadrupole (DQ_γ). For clarity, the defect configurations are shown by using different physical quantities. The black curves in plots (a) and (b) are illustrations of the defect lines determined from the isosurface of $S = 0.25$. (c) is a cross-section view $Q^2_{zz}(\mathbf{r})$ on the x-z plane where the far-field nematic director is along the z axis. (d), (e), and (f) are cross-section views of $Q_{xx}(\mathbf{r})$ on the x-z plane where the far-field director makes an angle $\gamma = 38.4^\circ, 0^\circ$ and $\gamma = 46.8^\circ$ from the z axis, respectively. (a) and (b) are produced from numerical solutions at $[\tau,\xi_R] = [-0.2234, 0.07209]$ ($R \approx 0.1\ \mu$m in 5CB). (c) and (d) are produced from numerical solutions at $[\tau,\xi_R] = [-0.2234, 0.007071]$ ($R \approx 1\ \mu$m in 5CB). (e) and (f) are produced from numerical solutions at $[\tau,\xi_R] = [-0.2234, 0.01179]$ ($R \approx 0.6\ \mu$m in 5CB).

Ravnik *et al.* [14]. The E state was reported by Araki and Tanaka [47] who numerically solved the hydrodynamic equation for the dimer problem based on the Landau-de Gennes theory for particles with radius $R = 25 \sim 60$ nm. Both E and O structures were found by Ravnik *et al.* for $R = 0.5\ \mu$m based on Landau-de Gennes theory [14]. Recently, the O state was also reported for nanoscale particles by using molecular simulations [61]. Experimentally, the E and O structures were observed by Ravnik *et al.*, who used laser tweezers to manipulate and assemble a pair of glass microspheres with radius $R = 2.35$ and $9.5\ \mu$m in 5CB liquid crystal cells with thickness from $5{-}22\ \mu$m [14]. They also demonstrated that the same mechanics can lead to the formation of colloidal wires from multiple particles.

The bubble-gum configuration is rather metastable, which was observed in an experiment for particles with radius $R = 5\ \mu$m by Poulin *et al.* [19]. The other three, D_γ, DQ_0, and DQ_γ, can be traced back to different combinations of single-particle structures, which were previously observed experimentally and some of which were addressed theoretically [11,15,16,62].

The phase diagram in Fig. 2 is determined by a comparison of the calculated free energies of different defect states. For example, each data point in Fig. 4(a) represents the free energy calculated after minimization with respect to $\mathbf{Q}$, D/R, and γ

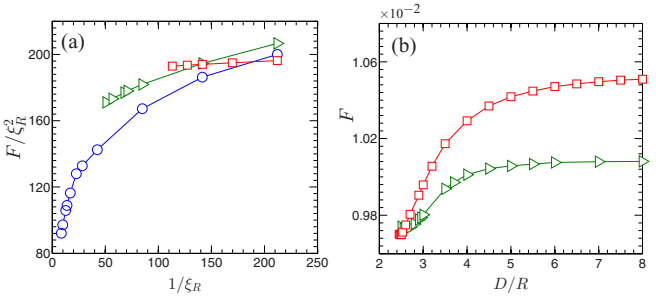

FIG. 4. (a) Reduced free-energy branches of U_γ (circle), D_0 (squares), and DQ_0 (triangles) as functions of $1/\xi_R$ at $\tau = -0.2234$, and (b) reduced free energies of D_0 (squares) and DQ_0 (triangles) obtained when D/R is fixed as a constraint at $[\tau,\xi_R] = [-0.2234,0.007071]$ ($R \approx 1\ \mu$m in 5CB).

for selected ξ_R and fixed $\tau = -0.2234$. The interpolation of the calculated data indicates that U_γ and D_0 branches cross each other at $1/\xi_R = 190.2$, which determines a single transition point on the U_γ-D_0 phase boundary in Fig. 2(e). The DQ_γ branch is always higher than the lower values of the other two, hence is deemed metastable.

The notion of stability and metastability, however, is relative. As an example, the kinetic pathway of reaching the stable D_0 state can go through the metastable DQ_0 formation. Figure 4(b) contains a description of the reduced free energies for both D_0 and DQ_0 as functions of D/R, when D/R is used as a constraint in the minimization procedure. In a single-particle phase diagram, this particular system is represented by a point to the left of the quadrupole-dipole transition line [see Fig. 1(g)]; hence at a large distance, the uncorrelated dipole-quadrupole pair, DQ_0, has a lower free energy than D_0's and can be regarded as more stable. As D/R decreases to a small distance, the defect structures start to interact. The D_0 state reaches a free-energy minimum approximately at $D/R = 2.5$, which has a lower value than that of the DQ_0 state at approximately $D/R = 2.6$. Both states experience defect-mediated attractions. In a real system, if its parameters can be adjusted to the left-hand side of the quadrupole-dipole transition line, one may observe a DQ_0-D_0 phase transition as the two spherical particles kinetically approach each other. Of course, whether a transition actually happens or the system remains at the DQ_0 metastable state in small D/R depends on the free-energy barrier between the DQ_0 and D_0 states, which is calculable through an advanced numerical procedure, for example the string method [84], but is beyond the scope of this paper. The difference between the two minima in Fig. 4(b) is about $2.2 \times 10^3\ k_BT$ in real units in terms of 5CB parameters.

V. FORMATION OF A COUPLED DIPOLE-DIPOLE STATE

The three most discussed dipole-dipole states are those with sphere-sphere center vector in parallel with the far-field nematic director, $\gamma = 0$ [22,44]. Shown in Figs. 5(a)–5(c) are cross-section plots of Q_{xx} of these configurations at $[\tau,\xi_R] = [-0.2234,0.007071]$ (corresponding to $R \approx 1\ \mu$m in 5CB), for fixed $D/R = 4$ and $\gamma = 0$. In this work, the stability of a configuration is assessed by a study of the

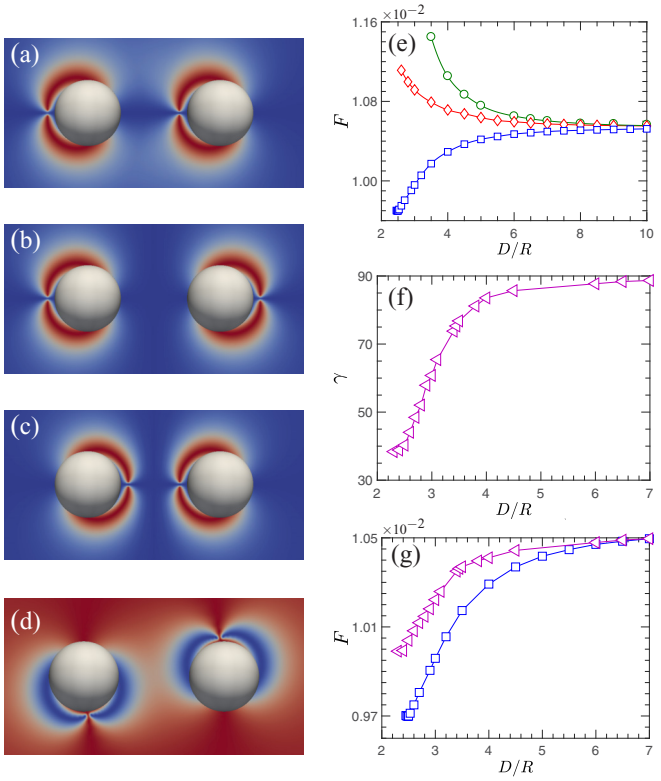

FIG. 5. (a)–(d) Three possible dipole-dipole configurations at $\gamma = 0$ (parallel, *p-p* type antiparallel, and *h-h* type antiparallel) and D_γ configuration for $D = 4R$ shown by Q_{xx}, (e) reduced free energies F calculated as functions of D/R for the first three configurations [squares, diamonds, and circles for (a), (b) and (c)], (f) optimal γ determined when the free energy is minimized with a D/R-constraint in the D_γ state, and (g) reduced free energies of D_γ (triangles) and D_0 (squares) as functions of D/R. The configuration in (d) has $\gamma = 83.6°$. All figures are produced from numerical solutions at $[\tau,\xi_R] = [-0.2234,0.007071]$ ($R \approx 1\ \mu$m in 5CB); in this example, the free energy at the reduced units 1×10^{-4} corresponds to about $8.3 \times 10^3\ k_BT$.

numerical solution for the free-energy difference

$$\Delta F(D/R,\gamma) = F(D/R,\gamma) - F(D/R = \infty,\gamma) \qquad (20)$$

as a function of both D/R and γ, where $F(D/R = \infty,\gamma)$ is the sum of the free energies of two single-sphere solutions at the same $[\tau,\xi_R]$, which is γ independent.

The parallel configuration in Fig. 5(a), D_0, always has a negative $\Delta F(D/R,0)$, implying a nematic-fluid-induced attraction between the two spheres, consistent with the results provided by Fukuda *et al.* [44] on the basis of the same model for $[\tau,\xi_R] = [-0.054,0.005]$ at a higher temperature but with a similar particle size. As demonstrated in Fig. 5(e), a free-energy minimum is achieved at approximately $D/R = 2.5$, indicating a closely coupled equilibrium dimer configuration shown in Fig. 2(d). This parallel configuration, in which two particle-defect dipoles align in the head-tail arrangement, was experimentally observed in the seminal work of Poulin and his coworkers for μm-sized particle ($R = 1.6 \sim 5\ \mu$m) [7]. They have also demonstrated that the same mechanism can lead to additional binding of multiple spherical particles, as

the result of the mediated attractive force between parallel dipoles, forming a linear chain of colloids. An effective, particle-particle potential energy curve was later deduced by Takahashi *et al.* experimentally [22], for D_0 where the minimum appears between (2,3), similar to Fig. 5(e) here and Fig. 4 in Ref. [44].

As demonstrated by the plots in Fig. 5(e), the free-energy differences of the antiparallel configurations at fixed $\gamma = 0$, shown in Figs. 5(b) and 5(c), are all positive, which indicate that the spherical particles interact with each other through a nematic-fluid-mediated repulsion; hence a finite-D/R configuration cannot be stable at all in a free dimer system. On the other hand, using optical tweezers to manipulate a pair of polystyrene particles of size $R = 2.55\ \mu$m in liquid crystal MJ032358, Takahashi *et al.* were able to enforce antiparallel configurations to form experimentally at large distances [22]; they have directly observed that indeed these types of configurations experience solvent-mediated repulsion.

In the rest of this section, we highlight our successful determination of the stable D_γ state with a nontrivial γ (i.e., $\gamma \neq 0$ or $\pi/2$). This configuration, illustrated in Fig. 3(d), is not often discussed in the theoretical literature related to this topic. Experimentally, the D_γ state was first reported by Yada *et al.* in Ref. [11]. Using PS particles (radius: 7.5–15 μm) in a nematic liquid crystal (ZLI-4792 confined with a thickness 50 μm), they successfully manipulate the PS pair to arrive at D_γ with $\gamma \approx 30^\circ$. Inspired by their experiments and other related experimental studies [12,85], we conducted a series of computations according to the current model by placing dipoles at a fixed distance D/R in a D_{90} form as the starting point [see Fig. 5(d)]. The numerical solutions are obtained here in a procedure where the γ constraint is relaxed. Taking the particular set of $[\tau,\xi] = [-0.2234,0.007071]$ (corresponding to $R \approx 1\ \mu$m in 5CB), the optimal γ as a function of D/R is shown by triangles in Fig. 5(f). In this case, as a function of D/R, the free-energy minimum is located at $D/R = 2.3$, at which the optimal γ reaches a finite, nontrivial value of 38.4°. The final configuration is shown in Fig. 3(d).

Although previously not often addressed theoretically, binding of dipole dimers at a nontrivial γ has been observed in a number of other studies experimentally. Using multiple silica beads ($R = 1.16\ \mu$m) immersed in 5CB liquid crystal, Muševič *et al.* made a two-dimensional crystal of these beads formed according to a self-assembly physical mechanism that is similar to the strong binding in the D_0 and D_γ states [12]. Instead of using D_{90} as the initial condition, several groups used the *h*-*h* type configurations at large distance, which is unstable against a γ perturbation, as the starting point [15,22]. Škarabot *et al.*, for example, observed the kinetic binding pathway of two large silica spheres ($R = 1.16\ \mu$m), which leads to the final D_γ state in 5CB in a matter of 140 s [15]; they reported a final tilt angle $\gamma = 36^\circ$ by releasing two particles from a laser trap starting from a *h*-*h* type antiparallel configuration; Takahashi *et al.* measured the variation of γ as two polystyrene particles with radius $R = 2.55 \pm 0.1\ \mu$m in a nematic liquid crystal (MJ032358 with cell thickness of $h = 10\ \mu$m) bind from an initial *h*-*h* type antiparallel state from far distance to a final (meta)stable state with a distance D/R near 2.5; the final configuration has a $\gamma \approx 40^\circ$ [22]. All the final γ angles, depending on the experimental conditions, are qualitatively comparable to the value 38.4° determined by the current theoretical work.

In comparison with D_0, how stable is D_γ with a nontrivial γ? An example of the free energies are shown in Fig. 5(g), which demonstrates that D_γ has a negative free-energy difference, but is always higher than that of the axisymmetric solution, D_0; as it turns out, this is a general trend in other parameter regimes. According to this assessment, D_0 is more stable. Škarabot *et al.* have produced the effective particle-particle potentials as functions of D/R of two kinetic trajectories starting from the D_0 and *h*-*h* configurations by integrating the force-separation measurements from their optical-tweezer experiment. Their conclusion seems to be the opposite: D_0 state is less stable. The discrepancy may come from the confinement effect as their experiments were conducted in a 5CB cell with cell thickness of 6 μm. Indeed, some previous experiments have shown that in thicker nematic layers, dipoles tend to spontaneously form linear chains along the rubbing direction [7,10], while in thinner nematic layers, 2D dipolar colloidal crystals can form [12].

VI. FORMATION OF A COUPLED DIPOLE-QUADRUPOLE STATE

In this section, we examine the configurations when two spherical particles, initially accompanied by dipolar and quadrupolar defect patterns in the nematic fluid, approach each other. Within the parameter regime considered in Fig. 2, the two coupled dipole-quadrupole states can be metastable. Two solutions have been obtained for systems with a fixed $\gamma = 0$ by initially making different arrangements for the quadrupole and dipole directions [62]: with the center-to-dipole-defect-ring vector pointing towards and backwards from the quadrupole configuration, as illustrated in Figs. 6(a) and 6(b). We mainly discuss the case of $[\tau,\xi_R] = [-0.2234,0.01179]$ (corresponding to $R \approx 0.6\ \mu$m in 5CB) here; according to the phase diagram in Fig. 1(g), the single-particle quadrupole and dipole states are stable and metastable, respectively, near this point in the phase diagram. Again, the stability of these configurations are evaluated by an examination of the free-energy difference defined in (20).

The reduced free energy as functions of the interparticle distance D/R are shown in Fig. 6(d) for the two configurations [Figs. 6(a) and 6(b)]. The free-energy difference of configuration (b) is always positive, indicating that the nematic-fluid-mediated interaction is repulsive for all D/R. Hence, configuration (b) is unstable. In contrast, the free-energy difference of configuration (a) (a DQ_0 state) is always negative, hence the nematic-fluid-mediated interaction is attractive. A free-energy minimum is achieved at approximately $D/R = 2.6$ in the second case. Corresponding to this distance, the optimal configuration is shown in Fig. 3(e). The physical picture present here is consistent with that provided by Kishita *et al.* on the basis of the same model at $[\tau,\xi_R] = [-0.054,0.005]$, and with their experiments in which latex particles with radius $R = 2.55 \pm 0.1\ \mu$m were used in a 20 μm liquid-crystal film [62]. Strictly speaking, the original quadrupole configuration is not exactly quadrupole anymore; there is a weak polarity in the surrounding nematic fluid, induced by the interaction with the

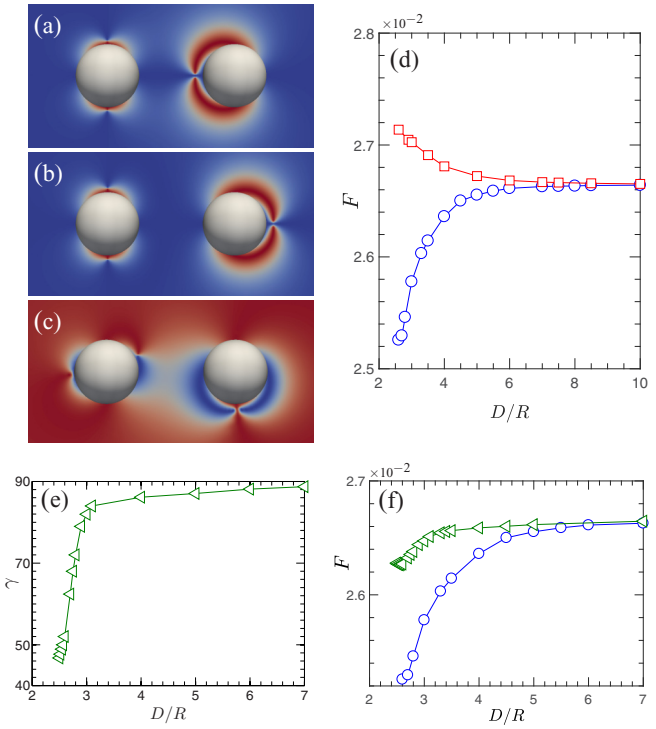

FIG. 6. (a)–(b) Two possible configurations of dipole-quadrupole pair aligned with $\gamma = 0$ for $D = 4R$ (shown by a Q_{xx} plot), (c) DQ_γ configuration shown by a Q_{xx} plot for $D = 4R$, (d) reduced free energies F as functions of D/R for the first two configurations [circles for (a) and squares for (b)], (e) the optimal γ for DQ_γ at a given D/R, and (f) the reduced free energies as functions of D/R for DQ_γ [triangles] and DQ_0 [circles]. All figures are produced from numerical solutions at $[\tau,\xi_R] = [-0.2234,0.01179]$ ($R \approx 0.6\ \mu$m in 5CB); in this example, the free energy at the reduced units 1×10^{-4} corresponds to about $1.8 \times 10^3\ k_BT$.

dipole configuration, and the Saturn ring slightly moves away from the dimer center. The axisymmetric DQ_0 state is stable against small-γ perturbations, as tested by our computation.

In this paper we provide concrete numerical evidence that an asymmetric state, DQ_γ with a nontrivial γ [Fig. 6(c)], is a solution to the free-energy model; this is a reminiscence of D_γ discussed in the preceding section. The configuration can be calculated from an initial condition in which the dipole and quadrupole axes are arranged to have a sideways direction from the far-field director, $\gamma = 90°$. This DQ_{90} state, however, is not stable and for fixed D/R, it converges to a configuration where a nontrivial γ angle always accompanies the free-energy minimum. As D/R decreases, the optimal γ shifts from $\pi/2$ to a smaller angle, eventually reaches $\gamma = 46.8°$ as the dimer finds an optimal distance $D/R = 2.5$. At this point, the free energy is minimized with respect to both γ and D/R. The final configuration is shown in Fig. 3(f), where the original Saturn ring is now strongly bent and moves to a new position.

On the experimental side, by conducting the experiments in wedge-type 5CB cells with thickness ranging from almost 0–8 μm, Ognysta *et al.* observed the convergence of two silica microspheres with radius $R = 2\ \mu$m originally arranged far away. Using the DQ pair as the template, they further assembled silica spheres in a higher-order, two-dimensional colloidal crystal; in such a case the defect lines are further distorted [16].

Figure 6(f) is an example of comparison between the free-energies of both DQ_γ and DQ_0. It indicates that DQ_0 is a more stable state than DQ_γ as it has a lower free-energy difference. Ravnik and Žumer also suggested that both states exist according to their study of the same Landau-de Gennes model [6] but did not provide the parameter stability region. By carefully searching through the parameter space, here we determine that both states are metastable rather than stable, strictly speaking, as the dipole-dipole D_0 or the quadrupole-quadrupole U_γ states have lower free energies, depending on the location of the parameters in the phase diagram, Fig. 2. On the other hand, the dimer system can be easily trapped into a metastable state by different kinetic pathways, hence both DQ_γ and DQ_0 are experimentally realizable [16].

VII. FORMATION OF A COUPLED QUADRUPOLE-QUADRUPOLE STATE

A. State stability

When a single spherical particle is immersed in a nematic fluid, the quadrupolar defect structure with a clearly defined Saturn-ring defect line is stable at low $1/\xi_R$. As we place two such particles in the same system, the two Saturn rings in the liquid crystal begin to interact and a number of possible structures containing entangled or decoupled defect lines occur [14,48].

A relatively simple case is to consider the interaction between two coaxial Saturn rings (CR) initially separated by a distance D with $\gamma = 0$ [see Fig. 7(a)]. Over the entire D/R range considered, as shown by the example in Fig. 7(h) the free-energy difference $\Delta F(D/R,0)$ always monotonically increases as D/R decreases. This indicates that such a configuration cannot exist in a real system and so far has not been observed without constraints.

In contrast, five defect structures were previously suggested when the separation vector of the two particles is constrained to make an angle $\gamma = \pi/2$ with the nematic director [14,48]. At a close distance, the defect lines interact and make exotic entangled defect lines, shown in Figs. 7(b)–7(f).

At a large distance, $\gamma = \pi/2$ requires that the two Saturn rings are coplanar and the defect rings around each particle are minimally influenced by each other. In most large-$1/\xi_R$ cases, the spherical pair experience a liquid-crystal mediated repulsion, as demonstrated by the free-energy plot in Fig. 7(g) (up triangles). This is consistent with the fact that R is hardly observed in real systems at a close distance, without further constraints.

In smaller-$1/\xi_R$ systems, the defect regions around the spheres are relatively extended; as the two spheres approach each other from a large distance, they experience a repulsion; however, at an intermediate distance, the portions of defect rings between the two spheres start to influence each other. At an even closer distance, these portions manifest into a single merged defect area to reduce the free energy. This results in an attraction, and the R state finally crosses over to H, as will be discussed in more detail below.

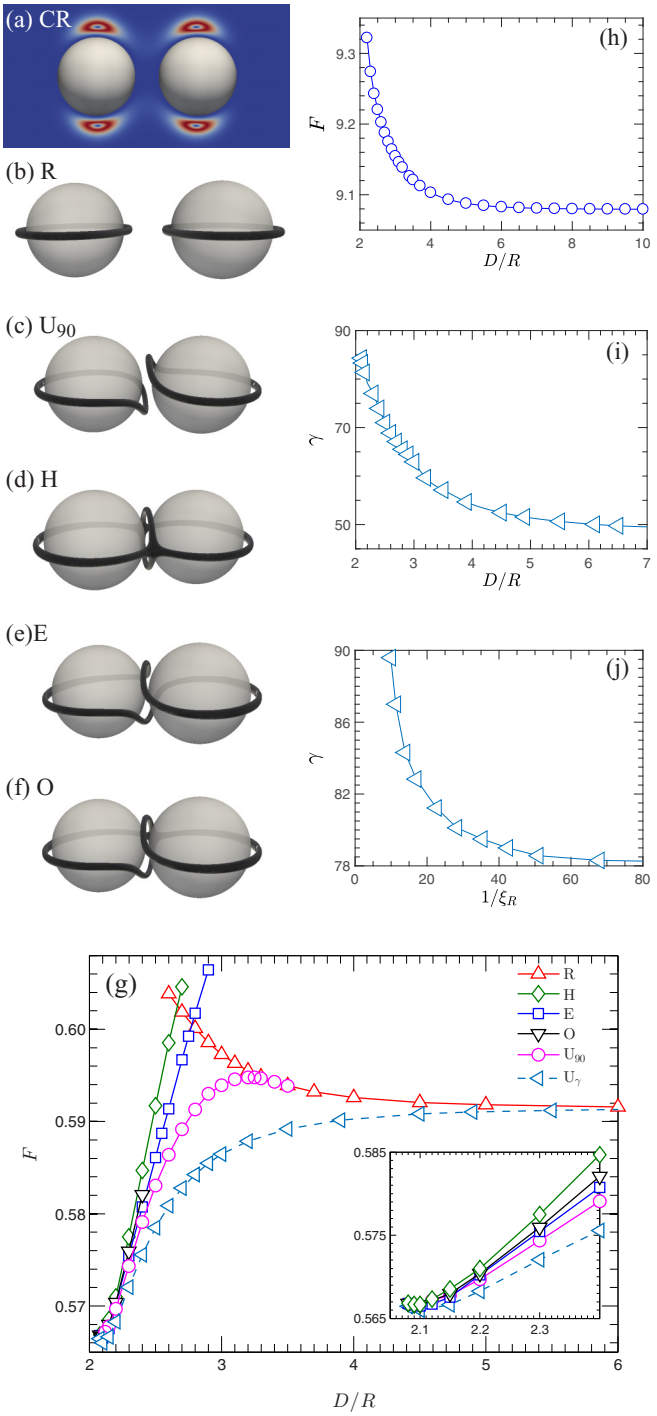

FIG. 7. (a)–(f) Illustration of CR, R, U_{90}, H, E, and O, (g) reduced free energies F of R, U_{90}, H, E, O and U_γ at $[\tau,\xi_R] = [-0.2234,0.07209]$ ($R \approx 0.1$ μm in 5CB), (h) reduced free energy of CR at $[\tau,\xi_R] = [-0.2234,0.3604]$ ($R \approx 20$ nm in 5CB), (i) optimal γ in U_γ at $[\tau,\xi_R] = [-0.2234,0.07209]$, and (j) optimal γ in U_γ as a function of $1/\xi_R$ for a fixed $D/R = 2.1$ at $\tau = -0.2234$. (a) is a β plot and (b)–(f) contain defect lines visualized by an isosurface $S = 0.25$. The inset shows the details of the minimum region in (g). In (g) and (h), the reduced free energies having a value 1×10^{-2} correspond to about 8.3×10^2 k_BT and 6.6 k_BT, respectively.

The R state is not sustainable at a small distance, and yields to the formation of other structures that have lower energies at low D/R. Enforced by the $\gamma = \pi/2 = 90^\circ$ constraint, a structure that bifurcates from the R state is an unentangled structure (U_{90}) where the portions of the two repulsive defect rings that are close to each other are strongly bent to avoid direct contact [Fig. 7(c)]. As shown in Fig. 7(g), at $[\tau,\xi_R] = [-0.2234,0.07209]$ (corresponding to $R \approx 0.1$ μm in 5CB), the bifurcation starts at approximately $D = 3.6\,R$, and ΔF dives into a negative territory as D decreases. During the process, near the bifurcation point, a very weak free-energy barrier exists.

The U_{90} state is obtained with a $\gamma = \pi/2$ constraint. Once the constraint is lifted, the Saturn-ring axes start to tilt and γ immediately moves away from $\gamma = \pi/2$ to form a U_γ state. Taking a static, far liquid-crystal field perspective, this means that the center-to-center vector of the two spheres starts to rotate. A new free-energy branch, shown in Fig. 7(g) by the left triangles, is reached by the system. The relationship between the optimal-γ and the interparticle distance D/R is displayed in Fig. 7(i) based on our numerical calculations, for $[\tau,\xi_R] = [-0.2334,0.07209]$ (corresponding to $R \approx 0.1$ μm in 5CB). As D/R decreases, a final free-energy minimum located approximately at $D/R = 2.1$ is reached and the optimal γ rises to $\gamma = 84.3^\circ$. A different calculation for $[\tau,\xi_R] = [-0.2334,0.01442]$ (corresponding to $R \approx 0.5$ μm in 5CB) yields a final equilibrium $\gamma = 78.3^\circ$, which agrees well with a recent experimental observation reported in Fig. 2 of Ref. [48], in which $\gamma = 79^\circ$. From another perspective, by fixing $\tau = -0.2334$ and $D/R = 2.1$, the evolution of the optimal γ can be seen as a function of $1/\xi_R$, shown in Fig. 7(j). It indicates that larger colloid particles have a more profound effect on the optimal value of γ.

The formation of entangled defect states has been extensively reported by both experimental observations and theoretical calculations [14,40,47,48,50,52]. The discovery of entangled topological defects opens a new field to study the topology of disclination lines [56,58,83,86,87]. In a nematic liquid crystal, the colloidal particles can be self-assembled into high-order structures by optimizing the entangled disclination lines, which form the nematic wires and braids [14,48,49,57]. In a chiral nematic liquid crystal, the disclination lines stabilized by arrays of colloidal particles can even form reconfigurable knots and links [87–89].

Based on the current study, we verify that defect lines that show entangled-hyperbolic-defect [H, Fig. 7(d)] (i.e., figure-of-theta [56,61,83]), figure-of-eight [E, Fig. 7(e)], and figure-of-omega [O, Fig. 7(f)] patterns, following the names adopted by previous authors [14,48], can indeed be stabilized for relatively large $1/\xi_R$ (from nanoscale to multi-μm-scale). An H structure has a mirror symmetry with respect to the x-z plane and contains two intersection defect points, as was also observed in previous studies base on the Landau-de Gennes theory [40,50,52]. The numerical calculations by Ravnik *et al.* for μm-sized particles indicate that the intersection of the defect loops only occurs with small particles [14]. Recently, the molecular simulations by Humpert *et al.* suggest that the intersection of the disclination lines for nanosized particles is a consequence of the time average over fluctuations among all entangled structures [61]. Both E and O structures are

chiral, breaking the mirror symmetry. At a fixed D/R value, all three states are stable against γ perturbations from $\gamma = \pi/2$, as the symmetry of the defect lines prefers such an optimal angle. Typical free-energy curves as functions of D/R can be found in Fig. 7(g) for $[\tau,\xi_R] = [-0.2234,0.07209]$ and have steep slopes before reaching minima. Hence, in a free state, each configuration is settled at its own free-energy minimum around $D/R = 2.1$. It can be noticed from the inset of Fig. 7(g) that the differences between the free-energy minima of all entangled and unentangled structures are quite small, less than $50\,k_BT$ for $R \approx 0.1\ \mu$m in 5CB. Although E, O (over the entire phase diagram in Fig. 2) and H (in a large area of of the phase diagram) have free-energy minima higher than that of U_γ, these structures are quite stable against both D and γ perturbations. As a consequence, they can be realized experimentally and an optical-tweezer experiment has demonstrated that stretching of the sphere-to-sphere separation D resulted in an observable increase in the stretching force [14].

B. Pathways in a fixed-γ system

Inspired by the optical-tweezer experiment, in this section we explore the structures that can be observable associated with a fixed $\gamma = \pi/2$ pathway. The assumption here is that structures can be manipulated through controlling the distance D. The demonstration of the pathway is based on the sequence of equilibrium profiles and not on a real kinetic simulation, which requires consideration of dynamic properties of the colloids, liquid-crystal solvent, and their mutual interaction on the surface.

Although to a large extent the intermediate observable states can be trapped in a particular defect state, it is helpful to establish the free energies of different branches for fixed $\gamma = \pi/2$. The precision of the current numerical approach allows us to analyze the fine details of the free energies, which enables us to construct a phase diagram in terms of $1/\xi_R$ and D, displayed in Fig. 8 at two fixed τ. The basic structures of these phase diagrams are similar. On nanosized particles, the molecular simulations by Humpert *et al.* show that transitions can occur between different states since the energy barriers between them are quite small [61]. In a previous study, using a Landau-de Gennes model, Tasinkevych and Andrienko showed that by decreasing D/R to a small value, rearrangements of topological defects can occur, going through transitions $U_{90} \rightarrow E \rightarrow H$ [51]. The same trajectory can be found in our phase diagram.

According to Fig. 8, the low-D and low-$1/\xi_R$ regime is where H (large area) and E (small area) phases can be stable. The free energy of the O state is always higher than the H or E state, hence is metastable only. In terms of 5CB parameters, the region where E can be stabilized has a small particle radius $0.3\ \mu$m, even at high temperatures. This, however, does not preclude the existence of entangled states in larger pairs of particles, as the system can be trapped in a metastable state (see pathways below). By switching to a 5CB nematic state abruptly from an isotropic state, Ravnik *et al.* produced all the entangled structures and U_γ for particles of radius $R = 19\ \mu$m in a $21\ \mu$m thick 5CB cell. Among their 124 quenching experiments, 48% were ended with U_γ and 36% were ended with E, only 3% were ended with H. Their experiments suggested that for μm-sized particles, U_γ is more stable than E, and E is more stable than H. The experiment reflects the fact that all the entangled structures are most likely to be metastable states for liquid crystals containing μm-sized particles, which is also supported by their numerical calculations, as all three entangled structures have higher free energy compared to the free energy of U_γ [14].

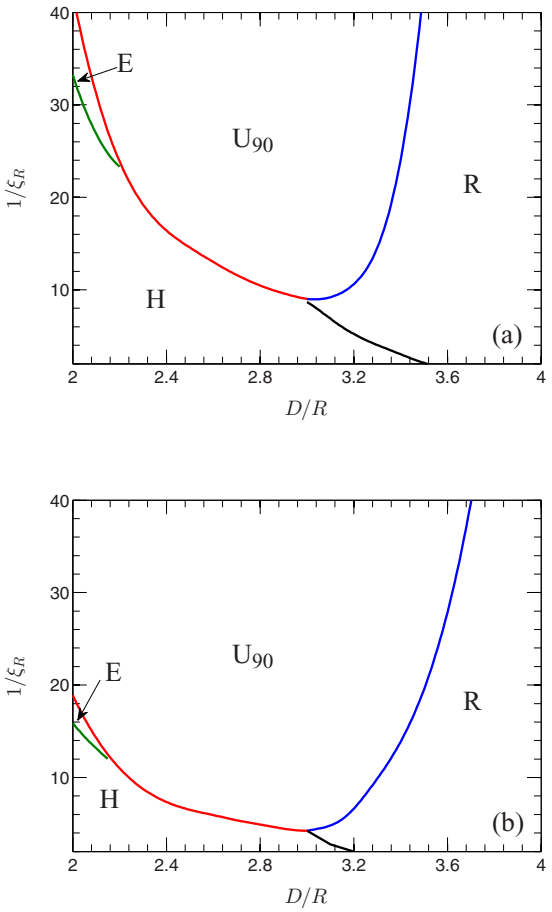

FIG. 8. Phase diagrams of energetically preferred configurations at a fixed $\gamma = \pi/2$ in terms of $1/\xi_R$ and D/R for fixed (a) $\tau = 0.0625$ and (b) $\tau = -0.2234$. The range $1/\xi_R = [0,40]$ approximately corresponds to $R = [0,0.3\ \mu\text{m}]$ in 5CB at a room temperature.

H-R pathway. This typically happens in a small-$1/\xi_R$ system, when H and R have a common phase boundary, shown in Fig. 8. When the two coupled spheres are stretched away from H, the free energy drastically increases, as demonstrated by Fig. 7(g) and by Fig. 9(b), along the H branch. While in a large-$1/\xi_R$ system the H and R branches are clearly defined separately [Fig. 7(g)], in a small-$1/\xi_R$ system they cross over to each other [Fig. 9(b)]. In the latter case, an extended domain of weakly varying singularity forms in the middle portion, which can be viewed as a crossover point to R. Both H and R share the same spatial symmetry, and the defect domain in the Q field follows this symmetry. As the particles are stretched even further, the free energy increases and the configuration now mainly resembles an R state. Once the system is settled in R, as the interparticle distance increases further, the free energy now decreases because of the fluid-mediated repulsive interaction.

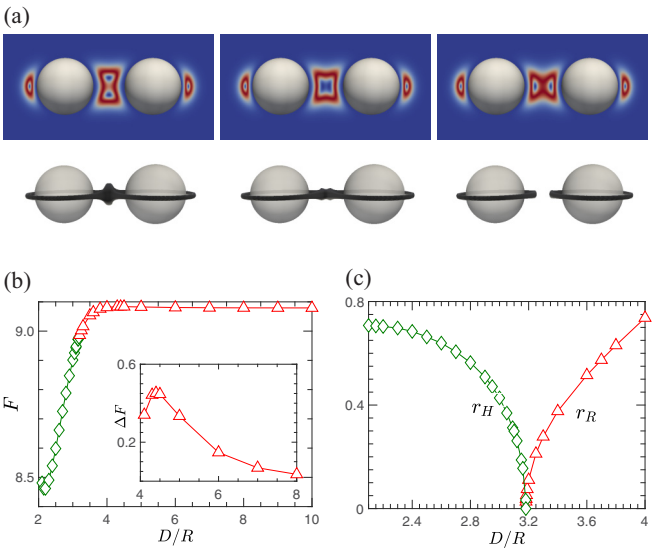

FIG. 9. (a) Illustration of the H-R pathway as the two particles in H are stretched apart, with distances from $D/R = 3.1, 3.2$, to 3.3, respectively, from left to right. (b) Corresponding reduced free energies of H (diamonds) and R (triangles) branches, and (c) behavior of the two order parameters defined for H (diamonds) and R (triangles). The calculation was performed for $[\tau,\xi_R] = [-0.2234,0.3604]$ ($R \approx 20$ nm in 5CB); with this choice, a free energy at the reduced units 1×10^{-2} corresponds to about 6.6 k_BT in 5CB. Shown in color are β plots. The defect lines are visualized by an isosurface $c_l = 0.05$.

A weak maximum in the free energy located at approximately $D/R = 4.4$ exists, shown in the inset of Fig. 9(b).

To demonstrate that indeed the H and R states are connected in this example, we consider two order parameters, which are specific to these configurations separately. On the x-z plane, we define a vertical radius r_H for the vertical ring at the center of the defect H structure. On the same plane, we define a horizontal distance r_R between the two nearest Saturn-ring intersections. These quantities are plotted in Fig. 9(c) by diamonds and triangles, respectively, where $r_R > 0$ for R and $r_H > 0$ for H. This plot clearly demonstrates that a crossover point at $D/R = 3.2$ exists.

H-U$_{90}$-R pathway. On the basis of Fig. 8, one can see that at a relatively small $1/\xi_R$, an H-U$_{90}$-R pathway is possible when the two spheres are stretched away from H. The properties of the H and R branches of the free energy are quite similar to those in the previous case; they make a smooth crossover. In the example shown in Fig. 10(b), the H (diamonds) and R (triangles) free energies are connected at approximately $D/R = 2.92$.

The appearance of the U$_{90}$ state, however, undermines this smooth connection and creates another possible scenario. In the example shown in Fig. 10(c), there is a free-energy branch that smoothly bifurcates from the R branch at approximately $D/R = 3.24$ and intersects with the H branch at approximately $D/R = 2.673$ [see the inset in Fig. 10(c)].

In order to define an order parameter for U$_{90}$, we consider the first diagonal element of the q_{lnm} tensor, denoted by $q_{lnm}^{(xx)}$, defined in the Appendix [see expansion (A3)]. Among positive m terms, one can show that all $q_{lnm}^{(xx)}$ terms with odd m vanish in

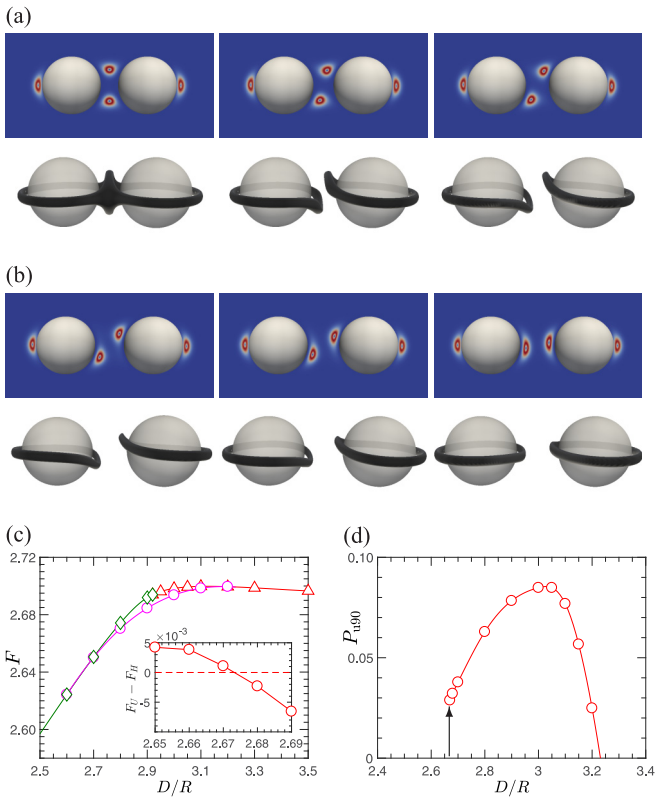

FIG. 10. Illustration of a possible two-stage transition when the particles in H is stretched away as D/R increase. The H state can make a first-order transition to jump into a U$_{90}$ state [shown in (a), where $D/R = 2.6$, 2.7 and 2.8, respectively, from left to right], and the U$_{90}$ state smoothly crosses over to R [shown in (b), where $D/R =$ 3,3.1 and 3.2, respectively, from left to right]. The H state could be trapped in its metastable form, directly makes an H-R transition described in Fig. 9. These transitions are assessed by the free energies displayed in (c), where diamonds, circles, and triangles represent data points calculated for the H, U$_{90}$, and R branches. The inset of (c) shows $F_U - F_H$ near the transition point. The order parameter for the U$_{90}$, P_{U90}, is displayed in (d). The system considered here has reduced parameters $[\tau,\xi_R] = [-0.2234,0.1768]$ ($R \approx 40$ nm in 5CB); with this choice, a free energy at the reduced units 1×10^{-2} corresponds to about 53 k_BT in 5CB. Shown in color are β plots. The defect lines are visualized by an isosurface $S = 0.2$.

H and R, due to the particular symmetries. On the other hand, because U$_{90}$ breaks the mirror symmetry of the director field with respect to the x-y plane, some of these terms survive. Hence, a characteristic measure for the U$_{90}$ state is $P_{U90} = \text{Max} q_{lnm}^{(xx)}$ where $m > 0$ and odd. Figure 10(d) is a plot of P_{U90} as a function of D/R. At the H-U$_{90}$ intersection, it makes a jump to a finite value (which is characteristic of a first-order phase transition) and at the U$_{90}$-R bifurcation point, it displays a continuous transition (which is characteristic of a second-order phase transition).

Here is a possible H-U$_{90}$-R pathway in two stages, shown in Fig. 10(a) and 10(b). At the first stage, the typical H defect pattern is stretched in the z direction until D/R reaches 2.7. Because of the first-order phase transition characteristics, the system can be trapped in the H state beyond this transition point. At a certain D/R, depending on the experimental

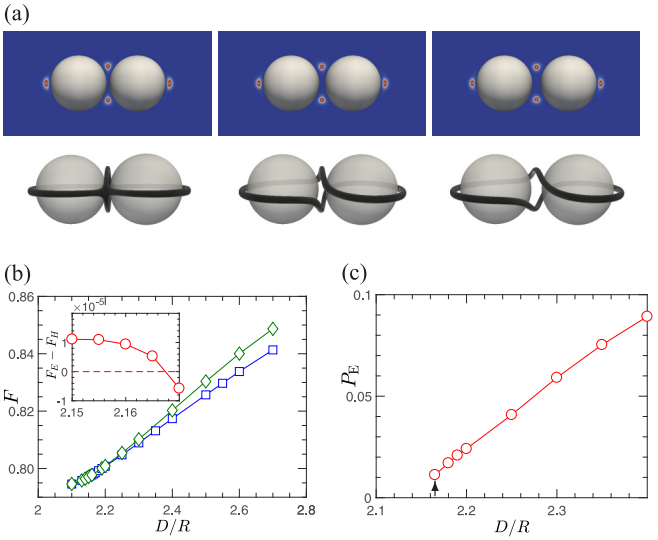

FIG. 11. (a) Illustration of a possible H-E pathway in a stretching experiment starting from H, where $D/R = 2.1$, 2.2, and 2.3, respectively, from left to right, (b) reduced free energies as functions of D/R for H (diamonds) and E (squares), and (c) the order parameter for E. The inset shows $F_E - F_H$ near the transition point. A jump in the order parameter exists after the two free energy curves cross each other. The calculation was performed for $[\tau,\xi_R] = [-0.2234,0.08839]$ ($R \approx 80$ nm in 5CB); with this choice, the free energy at the reduced units 1×10^{-2} corresponds to about $4.3 \times 10^2\, k_BT$ in 5CB. The defect lines are visualized by an isosurface $S = 0.25$.

condition, the H configuration can jump into a U_{90} configuration by lowering its free energy. As the particles are stretched further, at a distance $D/R = 3.24$, the bent rings recover their coplanar feature and the U_{90} state crosses over to the R state.

H-E pathway. Figures 8(a) and 8(b) show that in a narrow region for relatively large $1/\xi_R$, the E state is energetically stable. As a system in H is stretched away, crossing the H-E phase boundary, a possible H-E transition can occur, as illustrated in Fig. 11(a).

We take an example of relatively large $1/\xi_R$ and calculated the free energies of both states, shown in Fig. 11(b) by diamonds (H) and squares (E). As shown in details, the H and E branches cross each other at $D/R = 2.167$, indicating a first-order phase transition between the two states. Below this transition distance, the H branch has a lower value.

Again, we can define an order parameter for E by examining $q_{lnm}^{(xx)}$ on the basis of symmetry analysis. One can show that all $q_{lnm}^{(xx)}$ terms with negative m vanish in H, but some survive in E. Thus, a characteristic measure for E is $P_E = \mathrm{Max} q_{lnm}^{(xx)}$ where $m < 0$. A plot of P_E as a function of D/R can be seen in Fig. 11(c). At the free-energy crossing point, P_E jumps from 0 to a finite value. Hence, as a function of D/R, the H-E transition is first-order-like.

As the system crosses the first-order boundary, it can be trapped in the original state by maintaining its metastable state, without making a jump to another state. This explains the fact that both H and E states were experimentally stabilized and in a stretching experiment, the transition from H to E has not been observed to take place [14].

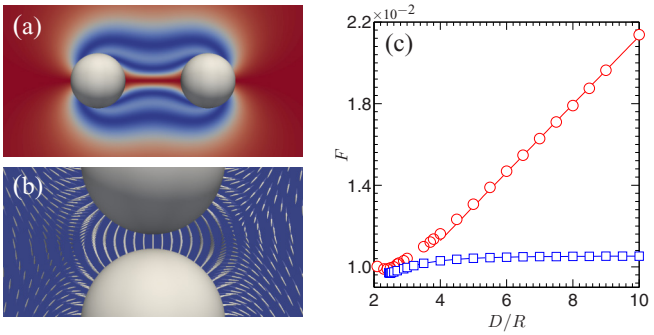

FIG. 12. (a) Orientational profiles in the bubble-gum configuration shown by Q_{zz}^2 plot at $D = 4R$, (b) detailed map between the two spheres at $D = 2.2R$ where the white ellipsoids are illustrated according to Q to display the main directors, and (c) reduced free energy F in B (circles), which can be compared with that of D_0 (squares). The example given here corresponds to a system having $[\tau,\xi_R] = [-0.2234,0.007071]$ ($R \approx 1$ μm in 5CB); with this choice, a free energy at the reduced units 1×10^{-4} corresponds to about $8.3 \times 10^3\, k_BT$.

VIII. BUBBLE-GUM CONFIGURATION

Poulin *et al.* unraveled a rather unique structure in the dimer case experimentally for particles with radius $R = 5$ μm [19]. The configuration, in which a defect line with a winding number -1 located at the center between the two spheres, does not originate from any single-particle configurations. Due to the resemblance of the orientational profile to a stretched piece of bubble gum, this state is referred to as a bubble-gum configuration (B) in the literature [see Fig. 12(a)]. The B state was later confirmed theoretically and experimentally to exist but is highly metastable and difficult to form in a nematic liquid crystal [22,46].

For completeness, we assessed the free energy of this configuration over the entire parameter space in Fig. 2(e). For example, a system at $[\tau,\xi_R] = [-0.2234,0.007071]$ (corresponding to $R \approx 1$ μm in 5CB) displays a free energy as a function of D/R that is always higher than that of D_0, shown in Fig. 12(c). In the large D/R region, the free energy displays a long-range linear behavior in D/R, which agrees with the previous experimental and theoretical results [19,22,46]. From the free-energy perspective, the B state is always metastable in a nematic liquid crystal.

In a related development, the recent experiment conducted by Tkalec *et al.*, places particles of radius $R = 2.36$ μm in a 10 μm $\pi/2$-twisted nematic cell, in which the defect structure shows a similar B pattern. The interaction potential also displays a long-range linear behavior, but the interaction is much stronger which by the end leads to the formation of 2D crystal structures [90]. The experimental results were also supported by their calculation based on the Landau-de Gennes theory [90].

IX. SUMMARY

The current state of the art in theoretical study of multiple colloidal particles in a nematic liquid crystal relies on the solution to the Landau-de Gennes theory. For the dimer problem, many conclusions have been drawn about the possible steady

states of the system, depending on the parameter regions. We task ourselves here to make a complete free-energy analysis over a significant range of variations of the system parameters τ and ξ_R, paying particular attention to the stabilities of various proposed and observed defect states by going through their competitive free energies.

We cover a large range of the coherence length scale ξ_R in the calculations, or more physically, a large radius range of the immersed particles, from nanoparticles to microparticles. All defect states are placed in one, comparative physical picture, backed up by a careful comparison of their free energies and a thorough analysis of their stabilities. In doing so, the physics of nontrivial γ states are explained in relationship with their relative states, exhaustively. The effects of temperature have not been carefully addressed before by theoretical studies. Our results indicate that it may be easier to realize the quadrupolar defects at higher temperatures, at which all interesting defect-defect phase transitions occur with a relatively larger R. Most experimental studies on these problems are based on optical methods, which are more suitable for observation of μm-sized structures. Only recently, by using some new experimental methods, such as video-tracking dark-field microscopy [27], have the direct experimental studies on the nanoscale particles in liquid crystals become possible. Several studies have been devoted to measuring the pair interaction between nanoparticles in a nematic fluid [24,27,29].

We devote a large part of this paper to the behavior of a colloidal-particle pair stretched away from their equilibrium states. The transitions among several states are described as kinetic pathways, as they either are already experimentally observed or offer further opportunities in future experimental probing. As the interparticle, center-to-center vector becomes another decisive system parameter, the interplays between stability and metastability display a full range of possibilities. The indication of first-order phase transitions between some of these states reveals the fact that some defect states are trapped in their own free-energy minima and have difficulties to overcome the energy barrier to jump to other states.

Our numerical study is conducted in an infinite space, free of finite-size effects of the confining box on the liquid crystal. This idealized approach is similar to the one adopted by Refs. [34–36,39,43–46,62,72], and enables us to focus on the effects due to the reduced temperature and particle size. However, in the real experiments, the liquid crystals are usually placed in a finite cell where the finite confinement size can alter the physical picture, as has been addressed by Refs. [9,17,21,37,41,63–66]. For example, a number of experimental and theoretical studies demonstrated that the quadrupolar structure appears to be more stable in a thin nematic cell [9,12,17,37,41]. Placing particles with radius $R = 1.16$ and $2.35\,\mu$m in a wedge-type 5CB cells with a thickness range from almost 0–8 μm, Škarabot *et al.* found that in the thinner wedge, the defect patterns are all quadrupolar, and in the thicker wedge, all dipolar [17]. More recently, an interesting experiment shows, by placing μm-sized particles near a wall with hills and dales that impose perpendicular anchoring, that the confinement can drive the topological transitions from Saturn rings to dipoles in deep wells [63]. The experimental study by Ref. [21] shows that the interaction potential decreases exponentially with the decay length proportional to the sample thickness, when the particle-particle separation goes beyond the cell thickness. This behavior has been explained in several later theoretical studies [64–66]. In the multiple-particle case, it has been shown experimentally that with large cell thickness, dipoles tend to spontaneously form linear chains along the rubbing direction [7,10], while with thinner nematic layers, 2D dipolar colloidal crystals can form [12]. Studying the confinement effects within our numerical approach is possible, but brings in another dimension in the parameter space. A systematic study of confinement effects will be an interesting future direction.

Another interesting direction that has been taken in recent years is to explore the formation of superstructures in these systems. The liquid-crystal-mediated interactions are instrumental for self-assembly of multiple colloidal particles to form a linear chain [7], two-dimensional colloidal crystals [12,15,16] and three-dimensional colloidal crystals [18,57]. The numerical technique developed here paves the way for further theoretical study of high-order structures.

We focus on the defect structures induced by spherical particles in a nematic liquid crystal. In recent years, attention has also been paid to the defect structures induced by particles with complex shapes and topologies in nematics and other states of liquid crystals, such as chiral nematic, blue phases, and smectics [23,87–89,91–99]. Solving the Landau-de Gennes model for these cases brings new computational challenges. It would be worthwhile to explore these problems by extending the computational strategies developed in this paper.

ACKNOWLEDGMENTS

We acknowledge the financial support from National Natural Science Foundation of China (Grants No. 11421101 and No. 11421110001), and an International Research Partnership Grant from the University of Waterloo that seeded this collaboration.

APPENDIX: NUMERICAL METHODS

The basic structure of the current numerical approach consists of three steps: (i) appropriate identification of the coordinate system for easy incorporation of the underlying geometry, (ii) expansion of the unknown function $\mathsf{Q}(\mathbf{r})$ in terms of special functions so that the expansion coefficients can be used as variational parameters, and (iii) the actual minimization of the free energy with respect to these variational parameters.

1. Coordinate system for two spherical particles

In the case of the two-particle problem, we use the bispherical coordinates, which were previously shown to be useful for description of the geometry composed of either a sphere and a nonintersecting infinite plane or two spheres [44,100,101].

To start, we represent a space point $\mathbf{r}$ by the standard cylindrical coordinates (ρ,z,ϕ). Then the transformation between the bispherical coordinates (ξ,μ,φ) and the cylindrical coordinates is given by

$$\rho = \frac{a\sin\mu}{\cosh\xi - \cos\mu}, \quad z = \frac{a\sinh\xi}{\cosh\xi - \cos\mu}, \quad \phi = \varphi. \tag{A1}$$

The parameter used in the transformation is $a = \sqrt{(D/2)^2 - R^2}$.

At a fixed φ, the bispherical coordinates map the infinite region in Cartesian coordinates onto a rectangle in the (ξ,μ) space, bounded by $-\xi_0 \leqslant \xi \leqslant \xi_0$ and $0 \leqslant \mu < \pi$, where $\xi_0 = \cosh^{-1}(D/2R)$ is a constant. One can show that $\xi = \mu = 0$ corresponds to infinity, and that the surface of constant ξ represents a sphere given by

$$x^2 + y^2 + (z - a\coth\xi)^2 = \frac{a^2}{\sinh^2\xi} \tag{A2}$$

in a Cartesian system. The surfaces of the two spherical colloids are represented by $\xi = \pm\xi_0$, respectively. For computational convenience, we further introduce $\zeta = \xi/\xi_0$, which renders the variable ranges for ζ, μ, and φ to be $[-1,1]$, $[0,\pi]$, and $[0,2\pi]$.

2. Spectral approximation

The description of the nematic structure is governed by the tensor function $\mathsf{Q}(\mathbf{r})$, which is expanded in terms of special functions: real spherical harmonics of (μ,φ) and Legendre polynomials of ζ. We write

$$\mathsf{Q}(\mathbf{r}) = \sum_{l=0}^{L-1}\sum_{n=|m|}^{N-1}\sum_{m=1-M}^{M-1} \mathsf{q}_{lnm} P_l(\zeta) Y_{nm}(\mu,\varphi), \tag{A3}$$

where L,N,M specify the truncation limits of the expended series, Y_{nm} are defined by

$$Y_{nm} = P_n^{|m|}(\cos\mu) X_m(\varphi), \tag{A4}$$

where P_n^m $(m \geqslant 0)$ are the normalized associate Legendre polynomials and X_m are defined by

$$X_m(\varphi) = \begin{cases} \cos m\varphi & m \geqslant 0, \\ \sin|m|\varphi & m < 0. \end{cases} \tag{A5}$$

Out of 3×3 elements of the traceless matrix q_{lnm}, only five elements are independent, because of the symmetry of the original Q matrix.

Inserting the expression (A3) to (10) and (11), we obtain a free energy in (2) as a function of all these unknown elements of tensor parameters, q_{lnm}. The free-energy function is then minimized by using a standard optimization method, such as L-BFGS [76], which treats the independent elements of tensor q_{lnm} as variables.

The exact cutoff values of L,N,M used depend on the system parameters $[\tau,1/\xi_R]$. We use the general guideline that the produced free energy carries a precision that allows us to determine the phase boundaries in Figs. 1 and 2 with an error bar smaller than the sizes of the plotted symbols.

The solutions for the axisymmetric systems are relatively simple to calculate, as we can reexpress

$$\mathsf{Q}(\zeta,\mu,\varphi) = \mathsf{T}(\varphi)\mathsf{Q}(\zeta,\mu,0)\mathsf{T}'(\varphi). \tag{A6}$$

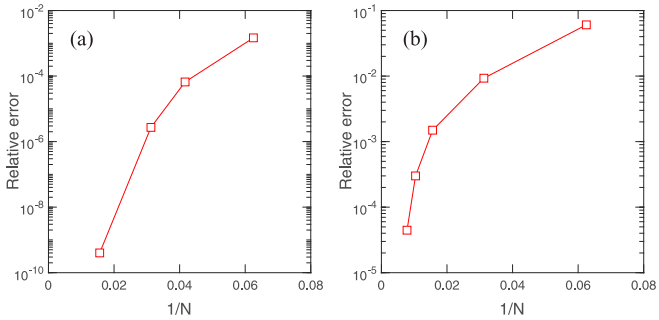

FIG. 13. Relative errors estimated for determination of the free energies in a single-particle problem. In (a), the quadrupolar solution was obtained at $[\tau,\xi] = [-0.2234, 0.07209]$ ($R \approx 0.1\ \mu$m in 5CB) with grid number up to $N = 128$. In (b), the dipolar solution was obtained at $[\tau,\xi] = [-0.2234, 0.01179]$ ($R \approx 0.6\ \mu$m in 5CB) with the grid number up to $N = 256$.

where

$$\mathsf{T}(\varphi) = \begin{pmatrix} \cos\varphi & -\sin\varphi & 0 \\ \sin\varphi & \cos\varphi & 0 \\ 0 & 0 & 1 \end{pmatrix}. \tag{A7}$$

Therefore, we can take $M = 3$. Figure 13 shows two numerical examples of the single-particle problem by letting $(N,L,M) = (N,N,3)$, in which we used grid number up to $N = 128$ and $N = 256$ as the reference solutions, respectively.

In general, larger L,N,M are required for larger $1/\xi_R$ and lower τ. For most nonaxisymmetric solutions presented here, we found that in small $1/\xi_R$ cases, the choice $(N,L,M) = (32,16,16)$ is adequate, and that in larger $1/\xi_R$ cases, the choice $(N,L,M) = (64,32,32)$ is required. Computationally, for $(N,L,M) = (64,32,32)$, the code runs at an efficiency of 3 s per L-BFGS step on a single-core CPU of 2.7 GHz clock speed. With a carefully choice of the initial guess, it takes less than 10^4 L-BFGS steps for a structure to converge.

3. Treatment of the far-field angle γ

The dimer case introduces two configurational parameters. The distance between the two spherical centers can be fixed by the use of the bispherical coordinates indicated above, along the z axis. The angle γ between the z axis and the far-field nematic director $\mathbf{n}_0$ is introduced by implementing the following trick. We decompose

$$\mathsf{Q}(\mathbf{r}) = \psi(\mathbf{r})\tilde{\mathsf{Q}}(\mathbf{r}) + \frac{S_0}{2}(3\mathbf{n}_0\mathbf{n}_0 - \mathsf{I}), \tag{A8}$$

where S_0 is the far-field orientational order parameter in (13). Instead of consideration of a spectral expansion of $\mathsf{Q}(\mathbf{r})$ on $\mathbf{r}$, we expand the elements of tensor $\tilde{\mathsf{Q}}$ on $\mathbf{r}$. The amplitude function $\psi(\mathbf{r})$ is imposed on the first term, which decays to zero at infinity. We take $\psi(r) = (\cosh\xi - \cos\mu)^{-\beta}$, where β is a prespecified parameter. The angle γ is introduced through $\mathbf{n}_0 \cdot \hat{z} = \cos\gamma$, where $\hat{z}$ is the unit vector in the z direction.

[1] P. G. de Gennes and J. Prost, *The Physics of Liquid Crystals* (Oxford University Press, Oxford, 1993).
[2] H.-R. Trebin, Adv. Phys. **31**, 195 (1982).
[3] M. Kléman, Rep. Prog. Phys. **52**, 555 (1989).
[4] M. Kléman and O. D. Lavrentovich, Philos. Mag. **86**, 4117 (2006).
[5] G. P. Alexander, B. G.-g. Chen, E. A. Matsumoto, and R. D. Kamien, Rev. Mod. Phys. **84**, 497 (2012).
[6] M. Ravnik and S. Žumer, Liq. Cryst. **36**, 1201 (2009).
[7] P. Poulin, H. Stark, T. C. Lubensky, and D. A. Weitz, Science **275**, 1770 (1997).
[8] O. Mondain-Monval, J. Dedieu, T. Gulik-Krzywicki, and P. Poulin, Eur. Phys. J. B **12**, 167 (1999).
[9] Y. Gu and N. L. Abbott, Phys. Rev. Lett. **85**, 4719 (2000).
[10] J.-C. Loudet, P. Barois, and P. Poulin, Nature (London) **407**, 611 (2000).
[11] M. Yada, J. Yamamoto, and H. Yokoyama, Phys. Rev. Lett. **92**, 185501 (2004).
[12] I. Muševič, M. Škarabot, U. Tkalec, M. Ravnik, and S. Žumer, Science **313**, 954 (2006).
[13] C. Völtz, Y. Maeda, Y. Tabe, and H. Yokoyama, Phys. Rev. Lett. **97**, 227801 (2006).
[14] M. Ravnik, M. Škarabot, S. Žumer, U. Tkalec, I. Poberaj, D. Babič, N. Osterman, and I. Muševič, Phys. Rev. Lett. **99**, 247801 (2007).
[15] M. Škarabot, M. Ravnik, S. Žumer, U. Tkalec, I. Poberaj, D. Babič, N. Osterman, and I. Muševič, Phys. Rev. E **76**, 051406 (2007).
[16] U. Ognysta, A. Nych, V. Nazarenko, I. Muševič, M. Škarabot, M. Ravnik, S. Žumer, I. Poberaj, and D. Babič, Phys. Rev. Lett. **100**, 217803 (2008).
[17] M. Škarabot, M. Ravnik, S. Žumer, U. Tkalec, I. Poberaj, D. Babič, N. Osterman, and I. Muševič, Phys. Rev. E **77**, 031705 (2008).
[18] A. Nych, U. Ognysta, M. Škarabot, M. Ravnik, S. Žumer, and I. Muševič, Nat. Commun. **4**, 1489 (2013).
[19] P. Poulin, V. Cabuil, and D. A. Weitz, Phys. Rev. Lett. **79**, 4862 (1997).
[20] I. I. Smalyukh, O. D. Lavrentovich, A. N. Kuzmin, A. V. Kachynski, and P. N. Prasad, Phys. Rev. Lett. **95**, 157801 (2005).
[21] M. Vilfan, N. Osterman, M. Čopič, M. Ravnik, S. Žumer, J. Kotar, D. Babič, and I. Poberaj, Phys. Rev. Lett. **101**, 237801 (2008).
[22] K. Takahashi, M. Ichikawa, and Y. Kimura, Phys. Rev. E **77**, 020703 (2008).
[23] C. P. Lapointe, T. G. Mason, and I. I. Smalyukh, Science **326**, 1083 (2009).
[24] M. Skarabot and I. Musevic, Soft Matter **6**, 5476 (2010).
[25] U. M. Ognysta, A. B. Nych, V. A. Uzunova, V. M. Pergamenschik, V. G. Nazarenko, M. Škarabot, and I. Muševič, Phys. Rev. E **83**, 041709 (2011).
[26] K. Izaki and Y. Kimura, Phys. Rev. E **87**, 062507 (2013).
[27] A. V. Ryzhkova and I. Muševič, Phys. Rev. E **87**, 032501 (2013).
[28] S.-J. Kim and J.-H. Kim, Soft Matter **10**, 2664 (2014).
[29] A. V. Ryzhkova, M. Škarabot, and I. Muševič, Phys. Rev. E **91**, 042505 (2015).
[30] E. M. Terentjev, Phys. Rev. E **51**, 1330 (1995).
[31] S. Ramaswamy, R. Nityananda, V. A. Raghunathan, and J. Prost, Mol. Cryst. Liq. Cryst. **288**, 175 (1996).
[32] R. W. Ruhwandl and E. M. Terentjev, Phys. Rev. E **55**, 2958 (1997).
[33] R. W. Ruhwandl and E. M. Terentjev, Phys. Rev. E **56**, 5561 (1997).
[34] T. C. Lubensky, D. Pettey, N. Currier, and H. Stark, Phys. Rev. E **57**, 610 (1998).
[35] H. Stark, Eur. Phys. J. B **10**, 311 (1999).
[36] H. Stark, Phys. Rep. **351**, 387 (2001).
[37] H. Stark, Phys. Rev. E **66**, 032701 (2002).
[38] B. I. Lev, S. B. Chernyshuk, P. M. Tomchuk, and H. Yokoyama, Phys. Rev. E **65**, 021709 (2002).
[39] J.-i. Fukuda, M. Yoneya, and H. Yokoyama, Phys. Rev. E **65**, 041709 (2002).
[40] O. Guzmán, E. B. Kim, S. Grollau, N. L. Abbott, and J. J. de Pablo, Phys. Rev. Lett. **91**, 235507 (2003).
[41] S. Grollau, N. L. Abbott, and J. J. de Pablo, Phys. Rev. E **67**, 011702 (2003).
[42] J. J. Feng and C. Zhou, J. Colloid Interface Sci. **269**, 72 (2004).
[43] J. Fukuda, M. Yoneya, and H. Yokoyama, Eur. Phys. J. E **13**, 87 (2004).
[44] J.-i. Fukuda, H. Stark, M. Yoneya, and H. Yokoyama, Phys. Rev. E **69**, 041706 (2004).
[45] J. Fukuda, H. Yokoyama, M. Yoneya, and H. Stark, Mol. Cryst. Liq. Cryst. **435**, 63/[723] (2005).
[46] J.-i. Fukuda and H. Yokoyama, Phys. Rev. Lett. **94**, 148301 (2005).
[47] T. Araki and H. Tanaka, Phys. Rev. Lett. **97**, 127801 (2006).
[48] M. Ravnik and S. Žumer, Soft Matter **5**, 269 (2009).
[49] M. Ravnik and S. Žumer, Soft Matter **5**, 4520 (2009).
[50] F. R. Hung, Phys. Rev. E **79**, 021705 (2009).
[51] M. Tasinkevych and D. Andrienko, Condens. Matter Phys. **13**, 33603 (2010).
[52] V. Tomar, T. F. Roberts, N. L. Abbott, J. P. Hernández-Ortiz, and J. J. De Pablo, Langmuir **28**, 6124 (2012).
[53] M. Tasinkevych, N. M. Silvestre, and M. M. T. da Gama, New J. Phys. **14**, 073030 (2012).
[54] T. Araki, F. Serra, and H. Tanaka, Soft Matter **9**, 8107 (2013).
[55] S. Alama, L. Bronsard, and X. Lamy, Phys. Rev. E **93**, 012705 (2016).
[56] S. Čopar and S. Žumer, Phys. Rev. Lett. **106**, 177801 (2011).
[57] S. Čopar, N. A. Clark, M. Ravnik, and S. Žumer, Soft Matter **9**, 8203 (2013).
[58] S. Čopar, Phys. Rep. **538**, 1 (2014).
[59] D. Andrienko, G. Germano, and M. P. Allen, Phys. Rev. E **63**, 041701 (2001).
[60] M. S. Al-Barwani, G. S. Sutcliffe, and M. P. Allen, J. Phys. Chem. B **108**, 6663 (2004).
[61] A. Humpert, S. F. Brown, and M. P. Allen, Liq. Cryst. (2017), doi: 10.1080/02678292.2017.1295478.
[62] T. Kishita, N. Kondo, K. Takahashi, M. Ichikawa, J.-i. Fukuda, and Y. Kimura, Phys. Rev. E **84**, 021704 (2011).
[63] Y. Luo, F. Serra, and K. J. Stebe, Soft Matter **12**, 6027 (2016).
[64] J. I. Fukuda and S. Žumer, Phys. Rev. E **79**, 041703 (2009).
[65] S. B. Chernyshuk and B. I. Lev, Phys. Rev. E **81**, 041701 (2010).

[66] O. M. Tovkach, S. B. Chernyshuk, and B. I. Lev, Phys. Rev. E **86**, 061703 (2012).
[67] J. Fukuda, J. Phys. Soc. Jpn. **78**, 041003 (2009).
[68] I. Bajc, F. Hecht, and S. Žumer, J. Comput. Phys. **321**, 981 (2016).
[69] J. Shen, T. Tang, and L.-L. Wang, *Spectral Methods: Algorithms, Analysis and Applications*, Vol. 41 (Springer, Berlin, 2011).
[70] J. C. Armas-Pérez, A. Londono-Hurtado, O. Guzmán, J. P. Hernández-Ortiz, and J. J. de Pablo, J. Chem. Phys. **143**, 044107 (2015).
[71] N. J. Mottram, and C. J. P. Newton, arXiv:1409.3542 [cond-mat.soft].
[72] T. Kishita, K. Takahashi, M. Ichikawa, J.-i. Fukuda, and Y. Kimura, Phys. Rev. E **81**, 010701(R) (2010).
[73] M. G. Forest, Q. Wang, and H. Zhou, Phys. Rev. E **61**, 6655 (2000).
[74] A. Majumdar, Eur. J. Appl. Math. **21**, 181 (2010).
[75] J. A. Moreno-Razo, E. J. Sambriski, G. M. Koenig, E. Diaz-Herrera, N. L. Abbott, and J. J. de Pablo, Soft Matter **7**, 6828 (2011).
[76] S. Wright and J. Nocedal, *Numerical Optimization*, Vol. 35 (Springer, Berlin, 1999).
[77] T. Mansaré, R. Decressain, C. Gors, and V. K. Dolganov, Mol. Cryst. Liq. Cryst. **382**, 97 (2002).
[78] P. G. de Gennes, C. R. Acad. Sci. Paris Ser. B **275**, 319 (1972).
[79] S. Mkaddem and E. C. Gartland, Phys. Rev. E **62**, 6694 (2000).
[80] A. C. Callan-Jones, R. A. Pelcovits, V. A. Slavin, S. Zhang, D. H. Laidlaw, and G. B. Loriot, Phys. Rev. E **74**, 061701 (2006).
[81] E. Penzenstadler and H.-R. Trebin, J. Phys. **50**, 1027 (1989).
[82] S. Kralj, E. G. Virga, and S. Žumer, Phys. Rev. E **60**, 1858 (1999).
[83] U. Tkalec and I. Muševič, Soft Matter **9**, 8140 (2013).
[84] Weinan E, W. Ren, and E. Vanden-Eijnden, Phys. Rev. B **66**, 052301 (2002).
[85] I. Muševič and M. Škarabot, Soft Matter **4**, 195 (2008).
[86] S. Čopar, T. Porenta, V. S. R. Jampani, I. Muševič, and S. Žumer, Soft Matter **8**, 8595 (2012).
[87] S. Čopar, U. Tkalec, I. Muševič, and S. Žumer, Proc. Natl. Acad. Sci. U.S.A. **112**, 1675 (2015).
[88] U. Tkalec, M. Ravnik, S. Čopar, S. Žumer, and I. Muševič, Science **333**, 62 (2011).
[89] V. S. R. Jampani, M. Škarabot, M. Ravnik, S. Čopar, S. Žumer, and I. Muševič, Phys. Rev. E **84**, 031703 (2011).
[90] U. Tkalec, M. Ravnik, S. Žumer, and I. Muševič, Phys. Rev. Lett. **103**, 127801 (2009).
[91] C. Bohley and R. Stannarius, Soft Matter **4**, 683 (2008).
[92] J. S. Lintuvuori, K. Stratford, M. E. Cates, and D. Marenduzzo, Phys. Rev. Lett. **105**, 178302 (2010).
[93] J. S. Lintuvuori, K. Stratford, M. E. Cates, and D. Marenduzzo, Phys. Rev. Lett. **107**, 267802 (2011).
[94] B. Senyuk, Q. Liu, S. He, R. D. Kamien, R. B. Kusner, T. C. Lubensky, and I. I. Smalyukh, Nature (London) **493**, 200 (2013).
[95] T. Machon and G. P. Alexander, Proc. Natl. Acad. Sci. U.S.A. **110**, 14174 (2013).
[96] A. Martinez, M. Ravnik, B. Lucero, R. Visvanathan, S. Žumer, and I. I. Smalyukh, Nat. Mater. **13**, 258 (2014).
[97] K. Stratford, O. Henrich, J. S. Lintuvuori, M. E. Cates, and D. Marenduzzo, Nat. Commun. **5**, 3954 (2014).
[98] A. Martinez, L. Hermosillo, M. Tasinkevych, and I. I. Smalyukh, Proc. Natl. Acad. Sci. U.S.A. **112**, 4546 (2015).
[99] S. Park, Q. Liu, and I. I. Smalyukh, Phys. Rev. Lett. **117**, 277801 (2016).
[100] J.-R. Roan and T. Kawakatsu, J. Chem. Phys. **116**, 7283 (2002).
[101] M. Ansorg, Phys. Rev. D **72**, 024018 (2005).